J. Fluid Mech. (2023), *vol*. 973, A27, doi:10.1017/jfm.2023.681

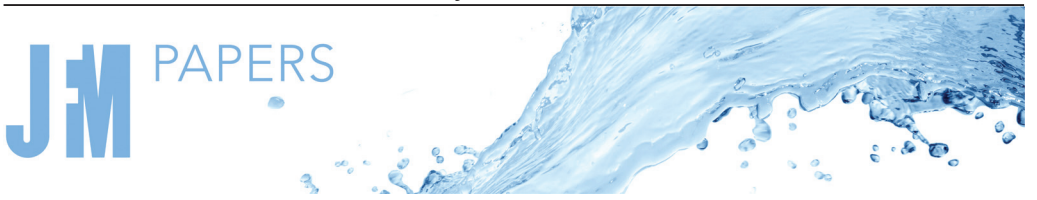

Interactions between oblique second mode and oblique waves in a high-speed boundary layer

Teng Zhou[1], **Zaijie Liu**[1], **Yuhan Lu**[1] **and Chao Yan**[1,†]

[1]National Key Laboratory of Computational Fluid Dynamics, Beihang University, Beijing 100191, PR China

(Received 12 February 2023; revised 4 August 2023; accepted 11 August 2023)

Interactions between oblique second mode and oblique waves at a high-speed boundary at Mach 4.5 are studied using linear stability theory, nonlinear parabolized stability equations (NPSE) and direct numerical simulation (DNS). Parametric analysis based on the NPSE suggests that the oblique second mode can amplify both the oblique first and second modes, with the former experiencing a higher amplification. Our analysis reveals that the mean-flow distortion and difference mode contribute to this enhancement, with the latter exerting a key influence through the parametric resonance process. Kinetic energy transfer analysis demonstrates that the oblique waves gain energy from the mean flow, rather than from the oblique second mode. Furthermore, we find that the mechanism underlying the interaction between a pair of second oblique waves and a single oblique wave is similar to that between an oblique second mode and an oblique wave, as the steady modes generated by the pair of oblique second modes have a limited impact on the oblique wave. Finally, DNS confirms the validity of two transition paths proposed in this study based on the NPSE results. The first path suggests that a pair of low-amplitude second oblique waves alone are insufficient to cause oblique breakdown, but the introduction of a pair of low-amplitude damping first oblique modes could lead to boundary layer breakdown. The second path involves the formation of a domino-like effect through the combination of different types of oblique waves with the appropriate parameters. These two nonlinear paths can lead to a fully developed turbulent boundary layer.

Key words: compressible boundary layers, transition to turbulence, nonlinear instability

1. Introduction

The laminar-to-turbulent transition is a critical issue in the design of high-speed vehicles, particularly for the thermal protection system (Zhao *et al.* 2022; Zhou, Liu & Yan 2023). However, our understanding of the nonlinear interactions of various modes during

† Email address for correspondence: yanchao@buaa.edu.cn

this transition is limited. The path of high-speed boundary layer transition is highly dependent on the free-stream environment (Morkovin 1969). The growth of acoustic, entropic or vortical disturbances (Fedorov 2003; Fedorov *et al.* 2013) can cause the laminar-to-turbulent transition of the boundary layer. When the disturbances are of small amplitude, linear stability theory (LST) (Mack 1984) accurately describes their evolution. At low-Mach-number supersonic boundary layers, the oblique first mode (Mack 1984), which is similar to the Tollmien–Schlichting waves in incompressible boundary layers, is the most amplified instability for the two-dimensional flat-plate boundary layer according to LST. As the Mach number increases ($Ma > 4.0$), the planar second mode, or Mack mode (Mack 1984), becomes dominant in the transition of the boundary layer.

When the amplitude of disturbances is high, nonlinear mechanisms can cause the boundary layer to break down. In incompressible flows, fundamental and subharmonic resonances were identified as the two nonlinear transition paths leading to the breakdown of the boundary layer (Kachanov 1994). However, the mechanisms of nonlinear interactions in high-speed boundary layers are more complex. Our understanding of these mechanisms is limited. For high-speed boundary layers, three relevant nonlinear transition paths have been identified: oblique breakdown (Mayer, Von Terzi & Fasel 2011; Hartman, Hader & Fasel 2021) and secondary instabilities (Herbert 1988; Ng & Erlebacher 1992) consisting of fundamental breakdown (K-type transition) (Sivasubramanian & Fasel 2015) and subharmonic breakdown (Chang & Malik 1994; Adams & Kleiser 1996). The oblique breakdown was first discovered by Thumm (1991) and Fasel, Thumm & Bestek (1993), and is initiated by the nonlinear interactions between a pair of oblique first modes with the same frequency and opposite spanwise wavenumbers in a supersonic boundary layer. Chang & Malik (1994) conducted a detailed study of the evolution stages of oblique breakdown using the nonlinear parabolized stability equations (NPSE). It is worth noting that the first mode is considered the most likely to dominate the transition mechanism for low-Mach-number supersonic boundary layers ($Ma < 3.5$) owing to the low initial amplitude requirements for oblique waves.

Fundamental and subharmonic breakdowns are two potential nonlinear mechanisms for high-Mach-number supersonic boundary layers ($Ma > 4.0$). These mechanisms arise from the interactions between a planar mode and a pair of oblique modes with the same frequency and opposite spanwise wavenumbers. The frequency of the oblique wave in the case of fundamental breakdown is the same as that of the planar mode, whereas for subharmonic breakdown, it is half that of the planar mode. Studies by Al-Salman (2003) have shown that the subharmonic between a planar second mode and a pair of first oblique modes can lead to a super-exponential amplification rate of the first mode. The spanwise wavenumber of the oblique wave is crucial in the interactions between a planar second mode and a pair of oblique waves with the same frequency as the second mode, according to Yu & Luo (2014). When the amplitude of the planar second mode is high, the nonlinear amplification rate of the oblique wave increases with an increase in the spanwise wavenumber. Franko & Lele (2013, 2014) used direct numerical simulation (DNS) to investigate the breakdown mechanism and heat transfer overshoot of the first mode oblique breakdown, second mode oblique breakdown and fundamental breakdown at Mach 6 with zero pressure gradient (ZPG) and an adverse pressure gradient (APG). They found that the breakup of streaks plays a significant role in the breakdown of the boundary layer for these three nonlinear paths, and that the APG increases the amplification rate of the initial amplitude, leading to an earlier transition. However, the breakdown mechanism for these three paths is similar between APG and ZPG. The fundamental breakdown is the most likely path to transition for a Mach 6.0 boundary layer at a flared cone, as found by

Hader & Fasel (2019). More recently, Meersman, Hader & Fasel (2021) investigated the effect of geometry, including straight and flared cones with zero attack, on the nonlinear stages of breakdown at Mach 6.0. The strong fundamental resonance was observed in both geometries, with the concave surface accelerating the transition process but not changing the mechanism for the streaks' evolution. It is important to note that these studies only investigated the mechanisms for interactions between a planar second mode and a pair of oblique waves with the same or half the frequency of the second mode. Further research is needed to study the interactions between the second mode and a wide range of oblique waves.

Maestrello, Bayliss & Krishnan (1991) found that the nonlinear interactions between the most unstable planar second mode and the most unstable oblique first mode can amplify both the nonlinearity and the three-dimensionality of spatially growing disturbances in the Mach 4.5 flat-plate boundary layer. To further examine these interactions, some researchers have focused on studying the evolution of wave packets or the evolution of random disturbances in high-speed boundary layers, aiming to identify the dominant nonlinear transition path or discover new transition paths. Leinemann, Hader & Fasel (2020, 2021) conducted a DNS to investigate the evolution of a small wave packet in the Mach 6.0 flat-plate boundary layer. They found that both the fundamental breakdown and the oblique breakdown can lead to the breakdown, but the dominant nonlinear transition is not clear. Further study is needed to better understand the interaction between the first and second modes. Unnikrishnan & Gaitonde (2020) introduced a planar second mode with low-amplitude random disturbances to the boundary layer through blowing and suction on the wall. They observed that the oblique waves were amplified and rode on the second-mode rollers, resulting in the breakdown of the boundary layer. This highlights the importance of the interaction between the second mode and oblique waves in the boundary layer.

In experiments, the nonlinear interactions between the different modes are often studied using particle image velocimetry, Rayleigh scattering visualization and pressure measurements. For example, Zhang, Tang & Lee (2013), Zhang *et al.* (2015) and Zhu *et al.* (2016, 2018) conducted a series of experiments on the transition process of a flared cone in a quiet wind tunnel. They found that the second mode can lead to fast breakdown of the boundary layer through the generation of vortical waves, and the interaction between the second mode and low-frequency mode was observed using bicoherence, which rapidly amplified the low-frequency waves. However, the mechanisms for these interactions are not clear, and there are challenges in studying the nonlinear region experimentally (Craig *et al.* 2019). Thus, numerical investigations are a more convenient method for studying the nonlinear mechanisms. The study by Chen, Zhu & Lee (2017) used stability analysis to explore the interactions between the planar second mode and low-frequency oblique waves. Results indicated that the low-frequency modes, known as Görtler vortices (Görtler 1954; Ren, Fu & Hanifi 2016), were most amplified by the planar second mode. However, the high amplitude of the low-frequency mode caused by the second mode weakened the amplitude of the second mode at the full-interaction stage. Additionally, the study observed parameter resonance between modes with specific frequencies and spanwise (azimuthal) wavenumbers and sum/difference modes. Similar work has also been conducted on the flat-plate hypersonic boundary layer by Zhang & Luo (2017) and Liu & Zhang (2019). These studies investigated the selective effect of the planar second mode on oblique waves and reported that low-frequency oblique modes or fundamental family disturbances are amplified more by the planar second mode, with the enhancement effect becoming stronger as the spanwise wavenumber of the oblique modes increases. These studies focused on the interactions between the planar second mode and oblique waves

and highlighted that not only can the fundamental and subharmonic breakdowns lead to boundary layer breakdown, but also the combination of the second mode with other frequencies can dominate the nonlinear transition path.

To the best of the authors' knowledge, the interactions between oblique second modes and oblique waves have received limited attention. This is primarily because the planar second mode is usually the most amplified disturbance in high-speed boundary layers. Nevertheless, it is important to note that the amplification rate of oblique second modes with small wave angles is comparable to that of the planar second mode (Husmeier & Fasel 2007; Zhou *et al.* 2022*b*). Additionally, the breakdown of a boundary layer is a three-dimensional process, and the oblique second mode can contribute to the three-dimensionality of the flow field, which cannot be achieved by the planar second mode. As a result, even when they have the same amplitude, the oblique second mode may trigger an earlier transition of the boundary layer than does the planar mode. In a recent study, Jahanbakhshi & Zaki (2019) found that the interaction between a pair of oblique second modes and a pair of oblique first modes can be the most dangerous disturbance at high energy levels of inlet disturbances, owing to the enhancement effect of the oblique second mode on the first oblique wave. Finally, interactions between pairs of second modes can result in the generation of steady modes (Pruett & Chang 1995; Franko & Lele 2013), making the interactions between oblique waves and these steady modes a topic worthy of further investigation. In addition, investigation of the interactions between oblique second modes and oblique waves has the potential to uncover new nonlinear pathways and provide valuable insights into the nonlinear pathways of transition in high-speed boundary layers.

The present study aims to investigate the interactions between oblique second mode and oblique waves in a high-speed boundary layer at Mach 4.5. The study is organized as follows: § 2 will describe the computational set-up and simulation methods. The results of the linear analysis will be presented in § 3. The interactions between a single oblique second mode and a oblique first or second mode will be examined using NPSE with parameter studies and kinetic energy budget analysis in § 4. A similar analysis of the interactions between a pair of oblique second modes and a single oblique first or second mode will be presented in § 5. Based on the results of §§ 3, 4 and 5, the study will explore two new nonlinear laminar-to-turbulent transition pathways in § 6 using DNS. The conclusion will be presented in § 7.

2. Simulation methods and computational set-up

2.1. *Direct numerical simulations*

The Navier–Stokes equations are the governing equations for the DNS in this study, which are in the form of

$$\frac{\partial \boldsymbol{Q}}{\partial t} + \frac{\partial \boldsymbol{F}_{c,j}}{\partial x_j} = \frac{1}{Re}\frac{\partial \boldsymbol{F}_{v,j}}{\partial x_j} \quad (j = 1, 2, 3). \tag{2.1}$$

The conservative variables $\boldsymbol{Q}$, convective flux vectors $\boldsymbol{F}_{c,j}$ and viscous flux vectors $\boldsymbol{F}_{v,j}$ in the DNS are described in more detail in Zhou *et al.* (2022*a*), and Re is the Reynolds number. These simulations are carried out using the OpenCFD code developed by Li *et al.* (2010*b*), which has been used to study high-speed boundary layer transitions (Li, Fu & Ma 2010*a*) and turbulent flows (Li *et al.* 2019). The convective terms are discretized spatially using an optimized sixth-order monotonicity-preserving scheme (Li, Leng & He 2013) combined with the Steger–Warming splitting method. The viscous terms are discretized using a sixth-order central difference scheme. A third-order Runge–Kutta method (Jiang & Shu 1996) is used for time advancement. The non-reflection and

supersonic outlet boundary conditions are used at the top and outlet of the computational domain, respectively. A no-slip isothermal wall is used at the bottom. Periodic boundary conditions are utilized on both sides of the domain. At the inlet, the profiles are solved using the compressible Blasius equations, validated in our previous study (Zhou *et al.* 2022*b*).

2.2. *Stability analysis*

As mentioned in § 2.1, the flow variables are described by the Navier–Stokes equations. To derive the governing equations of the fluctuation quantities, the flow variables $\phi = [\rho, u, v, w, T]$ can be divided into mean quantities $\bar{\phi} = [\bar{\rho}, \bar{u}, \bar{v}, \bar{w}, \bar{T}]$ and fluctuation quantities $\phi' = [\rho', u', v', w', T']$, where ρ, u, v, w and T are the density, streamwise velocity, wall-normal velocity, spanwise velocity and temperature, respectively. The mean quantities $\bar{\phi}$ are determined by the basic Navier–Stokes equations, while the fluctuations are calculated through stability analysis. The governing equations for the fluctuation quantities can be expressed as

$$\boldsymbol{\Gamma}\frac{\partial \phi'}{\partial t} + \boldsymbol{A}\frac{\partial \phi'}{\partial x} + \boldsymbol{B}\frac{\partial \phi'}{\partial y} + \boldsymbol{C}\frac{\partial \phi'}{\partial z} + \boldsymbol{D}\phi' + \boldsymbol{V}_{xx}\frac{\partial^2 \phi'}{\partial x^2} + \boldsymbol{V}_{yy}\frac{\partial^2 \phi'}{\partial y^2} + \boldsymbol{V}_{zz}\frac{\partial^2 \phi'}{\partial z^2} + \boldsymbol{V}_{xy}\frac{\partial^2 \phi'}{\partial x \partial y} + \boldsymbol{V}_{xz}\frac{\partial^2 \phi'}{\partial x \partial z} + \boldsymbol{V}_{yz}\frac{\partial^2 \phi'}{\partial y \partial z} = F. \tag{2.2}$$

The matrices $\boldsymbol{\Gamma}$, $\boldsymbol{A}$, $\boldsymbol{B}$, $\boldsymbol{C}$, $\boldsymbol{D}$, $\boldsymbol{V}_{xx}$, $\boldsymbol{V}_{yy}$, $\boldsymbol{V}_{zz}$, $\boldsymbol{V}_{xy}$, $\boldsymbol{V}_{xz}$ and $\boldsymbol{V}_{yz}$ are functions of the mean quantities $\bar{\phi}$. The nonlinear term F contains both the mean-flow and fluctuation variables. The expressions for the matrices and nonlinear term F can be found in Ren & Fu (2014).

2.2.1. *Linear analysis theory*

In LST, the mean quantities are solved for using the compressible Blasius equations (White 2006). This approach has been shown to give results in good agreement with those obtained through DNS as reported in Zhou *et al.* (2022*b*). The nonlinear term is not considered in the LST. Furthermore, it is assumed that the mean flow is quasi-parallel at a given location. The fluctuation quantities are assumed to be of the form

$$\phi' = \hat{\phi}(y)\exp(\mathrm{i}(\alpha x + \beta z - \omega t)), \tag{2.3}$$

where α, β and ω are the streamwise wavenumber, spanwise wavenumber and angular frequency, respectively. Substituting (2.3) into (2.2) and ignoring the lower-order terms and the wall-normal velocity of the mean flow, we can obtain the governing equations for the LST. The details of this derivation can be found in Chang (2004). The LST is solved as an eigenvalue problem, where the streamwise wavenumber α is a function of the spanwise wavenumber β and the angular frequency ω. In the spatial LST, both the spanwise wavenumber and the angular frequency are real, while the streamwise wavenumber $\alpha = \alpha_r + \mathrm{i}\alpha_i$ is complex. Given a fixed spanwise wavenumber and an angular frequency, we can determine the value of the streamwise wavenumber and the corresponding eigenfunction $\hat{\phi}$. The imaginary part α_i represents the amplification rate of the disturbance and a negative value of α_i indicates instability. The fourth-order central difference method is used for the wall-normal-direction discretization of the LST governing equations.

2.2.2. *Nonlinear parabolized stability equations*

In the NPSE, the form of disturbance is

$$\phi'(x, y, z, t) = \sum_{-M}^{M} \sum_{-N}^{N} \hat{\phi}_{mn}(x, y) \exp\left(\mathrm{i} \int_{x_0}^{x} \alpha_{mn}(x)\, \mathrm{d}x\right) \exp(\mathrm{i}(n\beta z - m\omega t)). \tag{2.4}$$

Substituting (2.4) into (2.2) and disregarding the second derivative of the mode shape function $\hat{\phi}_{mn}$ in the streamwise direction, we obtain the nonlinear parabolized stability equations for mode (m,n) as

$$\hat{D}_{mn}\hat{\phi}_{mn} + \hat{A}_{mn}\frac{\partial \hat{\phi}_{mn}}{\partial x} + \hat{B}_{mn}\frac{\partial \hat{\phi}_{mn}}{\partial y} + \hat{C}_{mn}\frac{\partial^2 \hat{\phi}_{mn}}{\partial y^2} = \hat{F}_{mn} \exp\left(-\mathrm{i} \int_{x_0}^{x} \alpha_{mn}\, \mathrm{d}x\right). \tag{2.5}$$

The details of the coefficient matrices and nonlinear terms F_{mn} in this equation can be found in Chang (2004). The calculation of the phase velocity for each mode is related to the real part of the streamwise wavenumber, which can be calculated as

$$c_{mn} = \frac{\omega_m}{\mathrm{Re}(\alpha_{mn})}. \tag{2.6}$$

The boundary conditions for each mode at the wall and far field are

$$y = 0 \text{ and } \infty : \hat{u}_{mn} = \hat{w}_{mn} = \hat{v}_{mn} = \hat{T}_{mn} = 0. \tag{2.7}$$

For the mean-flow distortion (0,0), the far-field boundary condition for the wall-normal velocity is (Chang & Malik 1994)

$$y = \infty : \frac{\partial \hat{v}_{00}}{\partial y} = 0, \tag{2.8}$$

which accounts for the evolution of the boundary layer. To solve for the shape function ϕ_{mn} and wavenumber α_{mn}, the wavenumber is updated as

$$\alpha^{new} = \alpha^{old} - \mathrm{i}\frac{1}{E}\int_0^{\infty} \bar{\rho}\left(u^*\frac{\partial \hat{u}}{\partial y} + v^*\frac{\partial \hat{v}}{\partial y} + w^*\frac{\partial \hat{w}}{\partial y}\right) \mathrm{d}y, \tag{2.9}$$

where

$$E = \int_0^{\infty} \bar{\rho}(|\hat{u}|^2 + |\hat{v}|^2 + |\hat{w}|^2)\, \mathrm{d}y \tag{2.10}$$

and superscript $*$ denotes the complex conjugate. The discretization of the NPSE in the wall-normal direction utilizes a fourth-order central difference method to accurately capture the flow dynamics. Furthermore, to maintain the stability of the calculations and prevent the residual ellipticity that can arise in numerical simulations, the streamwise direction is discretized using a first-order backward scheme with the Vigneron technique (Chang & Malik 1994). This approach has been proven to be effective in producing reliable and accurate results in previous studies. The base flow for the NPSE simulations is obtained by the DNS, in which the inlet disturbance is not included. The validation of DNS and NPSE solvers is conducted in the Appendix.

Ma_∞	Re (m^{-1})	T_∞ (K)	T_w/T_∞	γ	Pr
4.5	7.2×10^6	65.15	4.0	1.4	0.72

Table 1. Free-stream flow condition.

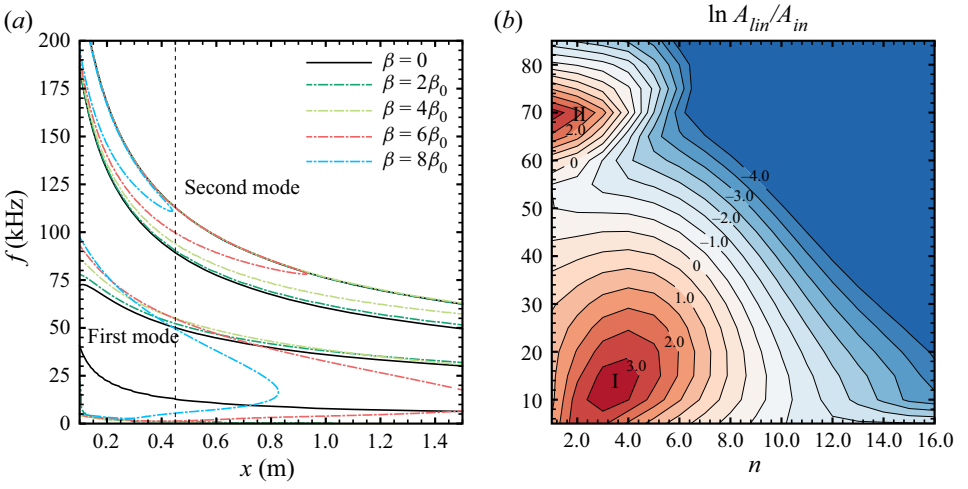

Figure 1. (*a*) Neutral curves obtained through linear stability analysis. (*b*) Contours of the linear amplitude, $\ln A_{lin}/A_{in}$, at $x = 1.025$ m, where A_{lin} is calculated using NPSE with only one oblique wave at the inlet. The first and second mode regions are labelled with Roman numerals I and II, respectively. The vertical dashed line indicates the inlet of DNS and NPSE.

2.3. *Computational set-up*

The current study focuses on a two-dimensional high-speed boundary layer and considers the fluid to be a perfect gas. The free-stream conditions are based on the high-altitude flight tests performed by Harvey (1978) and Schneider (1999), which have been proven to induce transition; see table 1. The viscosity of the fluid is calculated using Sutherland's law. The inlet of both NPSE and DNS is set at $x_{in} = 0.45$ m, where the boundary layer thickness is $\delta_{in} \approx 3.20 \times 10^{-3}$ m; see figure 1(*a*). For the simulation grids, the streamwise and spanwise distributions for DNS are equidistant, while the wall-normal direction for LST and NPSE uses 175 equidistant points, which is consistent with the DNS. The grid stretching in the wall-normal direction can be found in Zhou *et al.* (2021). The NPSE uses at least 12 points within a wavelength of the fundamental wave in the streamwise direction. The details of the domain size and grid resolution for the DNS will be presented in § 6.

3. Linear instability

The results of the linear stability analysis performed on a two-dimensional high-speed boundary layer at Mach 4.5 using the LST method are presented in figure 1(*a*). The fundamental frequency and spanwise wavenumber are defined as $f_0 = 5$ kHz and $\beta_0 = 83.8\,\text{m}^{-1}$, respectively. The relationship between the angular frequency and f (kHz) can be found in Mayer *et al.* (2011). In the following, the combination (m,n) represents a mode with frequency mf_0 and spanwise wavenumber $n\beta_0$. The analysis reveals the existence of

two unstable regions, referred to as the first and second modes (Mack 1984). It is observed that the first mode region increases and then decreases in size as the spanwise wavenumber increases, whereas the size of the second mode region decreases. Interestingly, when the spanwise wavenumber is $\beta = 2\beta_0$, the unstable region of the second mode is nearly identical to that when $\beta = 0$. This is due to the fact that the amplification rate of the oblique second mode with a small wave angle is comparable to that of the planar second mode (Husmeier & Fasel 2007). As an illustration, consider the real part of the streamwise wavenumber of the second mode (18,2) at the inlet, which is $\alpha_r = 844.06\,\mathrm{m}^{-1}$, and the corresponding wave angle is 11.23°.

To further explore the linear stability of the Mach 4.5 boundary layer, the NPSE simulations (neglecting nonlinear terms) are initiated with oblique waves (m,n) at the inlet of the domain. The frequency extends from $m = 1$ to $m = 17$ and the spanwise wavenumber ranges from $n = 1$ to $n = 16$, resulting in a total of 272 cases. The initial amplitude of the streamwise velocity fluctuations of each mode is $A_{in} = 10^{-5}u_\infty$ at $x_{in} = 0.45$ m. The contours of the amplitude of each oblique wave (f,β) at $x = 1.025$ m are displayed in figure 1(b), which shows that the value of $\ln A_{lin}/A_{in}$ is high in regions I and II, corresponding to the unstable first and second mode regions, respectively. Although the amplification rate of the second mode is higher than that of the first mode, the maximum value of $\ln A_{lin}/A_{in}$ is almost the same for both modes. This is due to the fact that the unstable first mode region is wider in the streamwise direction compared with the second mode region, as seen in figure 1(a). With an understanding of the linear stability of the Mach 4.5 boundary layer, the nonlinear interactions between the second mode and the broadband oblique waves will be discussed in the following sections.

4. Interaction between an oblique second mode and an oblique wave

4.1. *Parametric study*

For the parametric simulations, mode (18,2) is selected as the second mode because of its high linear amplification rate, which is very close to that of the planar second mode (18,0). In addition, it begins amplifying closer to the inlet than mode (14,0), which is amplified to higher amplitude at $x = 1.05$ m; see figure 1(a,b). The second mode (18,2) and an oblique wave (m,n) are initiated at the inlet of the domain with amplitudes of the streamwise velocity fluctuation set to $1.5 \times 10^{-3}u_\infty$ and $10^{-5}u_\infty$, respectively. The frequency extends from $m = 1$ to $m = 17$ and the spanwise wavenumber ranges from $n = 1$ to $n = 16$. In the NPSE simulations, only six modes are considered: the second mode (18,2), its harmonic (36, 4), the oblique wave (m,n), the difference mode ($18 - m$, $2 - n$), the sum mode ($18 + m$, $2 + n$) and the mean-flow distortion (MFD) (0,0). The main interactions can be listed as

$$(18,2) - (m,n) \rightarrow (18 - m, 2 - n); \tag{4.1}$$

$$(18,2) + (m,n) \rightarrow (18 + m, 2 + n); \tag{4.2}$$

$$(18 + m, 2 + n) + (18 - m, 2 - n) \rightarrow (36,4); \tag{4.3}$$

$$(18,2) + (18,2) \rightarrow (36,4). \tag{4.4}$$

It is worth noting that the interactions between the MFD and modes are also taken into account in the NPSE. After careful validation, it has been determined that this simple model is sufficient; see the Appendix. There are 272 cases covering 17 frequencies and 16 spanwise wavenumbers, which are same as those set in § 3. The amplitude of the streamwise velocity fluctuations of the other oblique wave is $10^{-5}u_\infty$. The wave angle

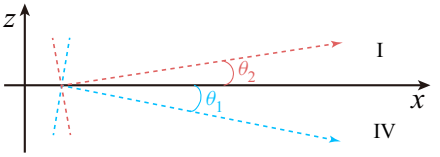

Figure 2. Diagram showing the direction of evolution of oblique waves. Here, θ_2 and θ_1 represent the wave angles of the oblique second mode and the other oblique wave, respectively. The first and fourth quadrants are designated as I and IV, respectively.

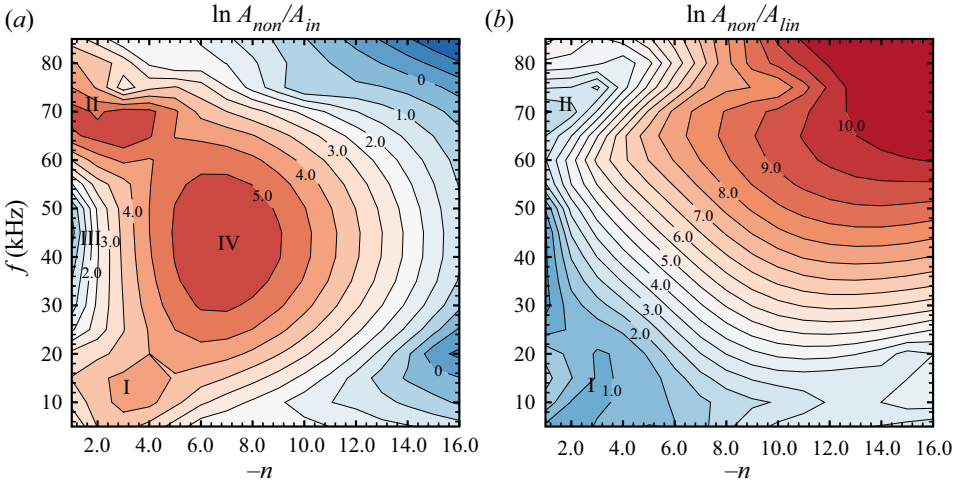

Figure 3. The contours of the amplitude of the oblique waves with negative spanwise wavenumber at $x = 1.025$ m: (*a*) contours of the nonlinear amplitude divided by the initial amplitude; (*b*) contours of the ratio of the nonlinear amplitude to the linear amplitude. The first and second mode regions are labelled with Roman numerals I and II, respectively, while Roman numerals III and IV indicate regions that are less and more amplified, respectively, compared with the initial amplitude.

is calculated as

$$\theta = \arctan \frac{\alpha_r}{\beta}, \tag{4.5}$$

where α_r and β represent the real parts of the streamwise and spanwise wavenumbers, respectively. There are two scenarios for the interactions between the oblique second mode and other oblique waves, as shown in figure 2. The first scenario is where the evolution direction of the other oblique wave is in the same quadrant as the second mode, and the second scenario is where the evolution directions of the two oblique waves are in different quadrants, as shown in figure 2. When the evolution direction of the oblique wave is in the fourth quadrant, the value of the spanwise wavenumber is negative. As the frequency and spanwise wavenumber of the second mode are fixed, the wave angle θ_2 of the second mode can be obtained through linear stability analysis and is set to a positive value in this study.

The results of the amplitude of the oblique wave with negative and positive spanwise wavenumbers in the n–f contours at $x = 1.025$ m are displayed in figures 3 and 4, respectively. When the spanwise wavenumber of the oblique wave is negative, almost all of the oblique waves, except those with a large spanwise wavenumber, are amplified compared with the initial amplitude; see figure 3(*a*). However, as seen in figure 3(*b*), all

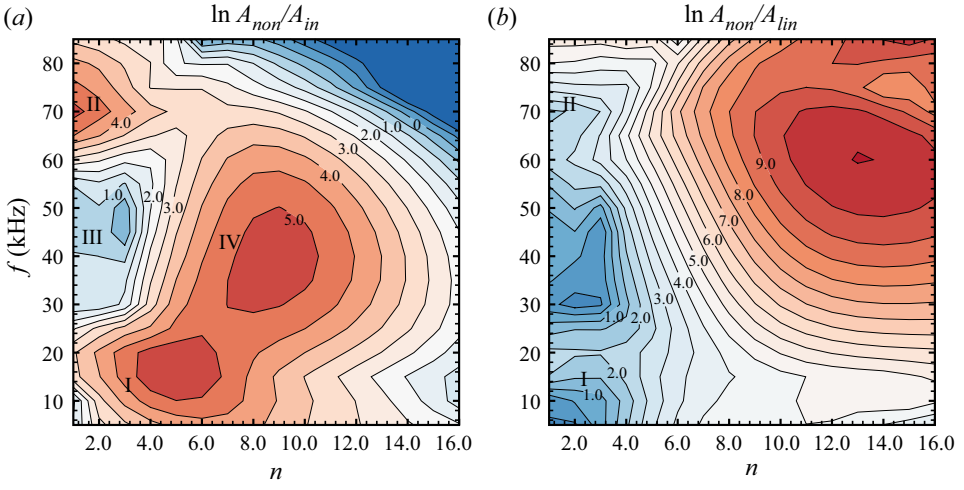

Figure 4. The contours of the amplitude of the oblique waves with positive spanwise wavenumber at $x = 1.025$ m: (*a*) contours of the nonlinear amplitude divided by the initial amplitude; (*b*) contours of the ratio of the nonlinear amplitude to the linear amplitude. The first and second mode regions are labelled with Roman numerals I and II, respectively, while Roman numerals III and IV indicate regions that are less and more amplified, respectively, compared with the initial amplitude.

of the oblique waves are amplified compared with the linear results, and oblique modes with a large spanwise wavenumber are amplified the most. This is due to the fact that the linear amplification rate of oblique waves with larger spanwise wavenumbers is damping, and the damping rate increases as the spanwise wavenumber increases, which will be further explained in the next section. Additionally, among the amplified oblique modes, the one with a frequency around 45 kHz and a negative spanwise wavenumber around -7 is the most amplified, as shown in region IV of figure 3(*a*). This is in contrast to the damping or low amplification rate seen in region IV of the linear results in figure 1. However, if the absolute spanwise wavenumber is less than 2.0, the oblique wave with a frequency around 45 kHz experiences less amplification, as indicated by region III in figure 3(*a*). Although the first and second modes exhibit high amplitudes in regions I and II, respectively, figure 3(*b*) shows that they are amplified weakly compared with the linear results.

The amplitude of oblique waves with a positive spanwise wavenumber at $x = 1.025$ m is presented in figure 4. In comparison with the oblique waves with a negative spanwise wavenumber shown in figure 3, there are some differences. Specifically, the absolute value of the spanwise wavenumber of the most amplified mode in region IV is greater than that in figure 3(*a*). The most amplified mode in figure 4(*a*) is (8,9), whereas in figure 3(*a*) it is (9,-7). However, in view of the wave angle difference with the oblique second mode, the most amplified modes are similar. The absolute initial wave angle difference between modes (18,2) and (8,9) is 51.2° as calculated using the parabolized stability equations, whereas the difference between modes (18,2) and (9,-7) is 49.5°. Thus, the wave angle difference between the second mode and the most amplified mode is around 50°. Overall, the distribution of the oblique wave's amplitude in figure 4 is similar to that in figure 3. Therefore, the results of the interaction between the second mode and an oblique wave with only a negative value are presented in the following.

To further understand the interaction of the oblique second mode with the first oblique waves, the evolution of modes with low frequencies $3f_0$, $8f_0$ and $9f_0$ is depicted in figure 5.

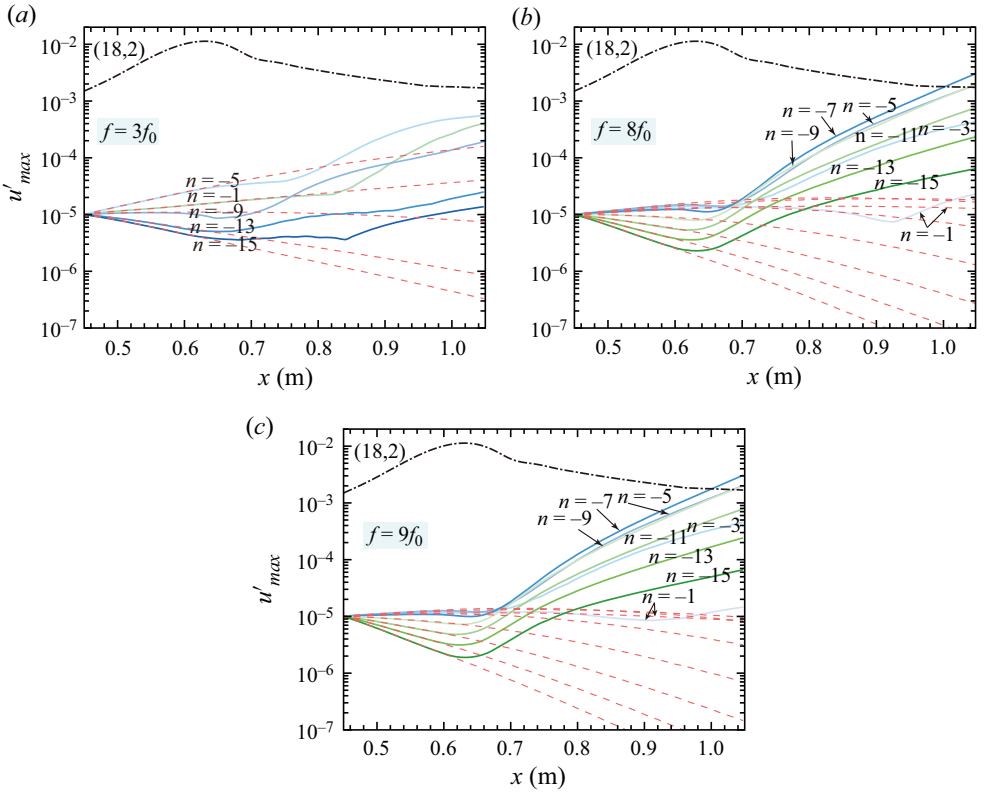

Figure 5. Amplitude evolution of oblique waves with constant frequency but different spanwise wavenumbers: (*a*) $f = 3f_0$; (*b*) $f = 8f_0$; (*c*) $f = 9f_0$. The red dashed lines indicate the linear evolution of the oblique waves.

These frequencies belong to the first mode, as shown in figure 1. As illustrated in figure 5, almost all the modes are amplified when the amplitude of the second mode (18,2) reaches its highest level at $x \approx 0.64$ m, even the damping modes. The amplitude of modes with frequency $3f_0$ is slightly increased. Modes with frequencies $8f_0$ and $9f_0$ grow rapidly, particularly those with a spanwise wavenumber around $n = -7$, which aligns with the results in figure 3. The reasons behind the promotion effects on the single first mode will be discussed in § 4.2. The interactions between the oblique second modes are shown in figure 6. For frequencies $14f_0$ and $16f_0$, the linear results indicate that the growth rate of these modes decreases with increasing spanwise wavenumber. The ratio of nonlinear amplitude to linear amplitude of the oblique waves with a larger spanwise wavenumber is more amplified than that with a smaller wavenumber. However, the amplitude of oblique waves with a larger spanwise wavenumber cannot surpass that of waves with a smaller wavenumber, as these higher wavenumbers decrease to much lower amplitudes before starting to grow rapidly. Similarly, the cause of rapid growth of the second mode will be discussed in § 4.3.

4.2. *Interactions between an oblique second mode and an oblique first mode wave*

It has been observed that almost all the oblique waves are amplified using NPSE. However, to determine the cause of the rapid growth of these waves, two possible paths are explored

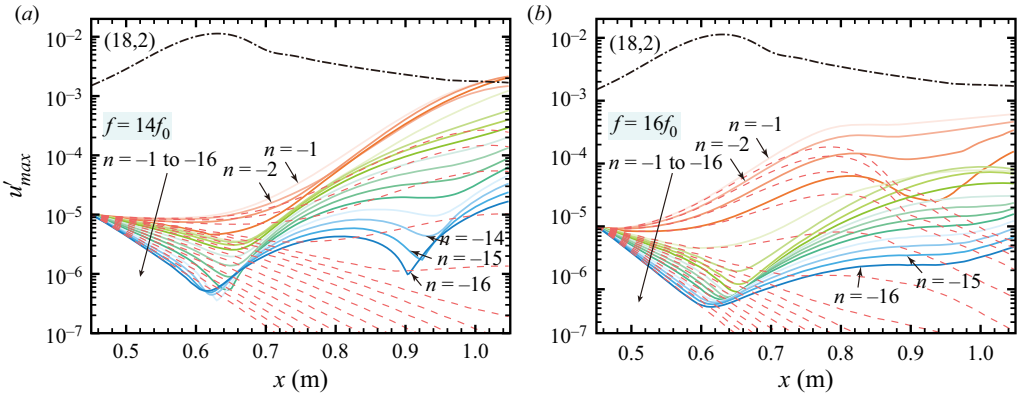

Figure 6. Amplitude evolution of oblique waves with constant frequency but different spanwise wavenumbers: (*a*) $f = 14f_0$; (*b*) $f = 16f_0$. The red dashed lines indicate the linear evolution of the oblique waves.

(Chen *et al.* 2017). The first path is the transfer of energy from the second mode to the oblique waves. The second path is the high amplitude of the second mode acting as a catalyst and allowing the oblique wave to gain energy from the mean flow. To further understand this phenomenon, mode (8,−10) has been selected as a representative single first mode to study in detail. The streamwise velocity amplitude of mode (8,−10) has been set to $10^{-4}u_\infty$. Additionally, six modes, along with their higher-harmonic modes, have been considered, resulting in a total of fifteen modes being analysed.

The evolution of the interaction between a first and a second mode is illustrated in figure 7(*a*). As seen in figure 7(*a*), the high amplitude of the mode (18,2) results in the rapid growth of the oblique wave (8,−10). Additionally, the slope of the amplification rate of the difference mode (10,12) is similar to that of the oblique wave (8,−10) at a downstream position of $x \approx 0.8$ m, which indicates that these modes are in resonance. The phase velocity of these modes is depicted in figure 7(*b*). It can be observed that the phase speeds of the modes (8,−10) and (10,12) are nearly the same at $x \approx 0.8$ m, suggesting that they are phase locked. The role of the difference mode (10,12) will be further discussed in § 4.2.2.

4.2.1. *Kinetic energy budget*

The kinetic energy equation, as described by Orszag & Patera (1983) and Hajj, Miksad & Powers (1993), is used to investigate the cause of the rapid growth of mode (8,−10). Based on the work of Chen *et al.* (2017), the streamwise momentum equations from (2.5) for each mode can be expressed as follows:

$$\bar{\rho}\frac{\mathrm{D}u}{\mathrm{D}t} = -L_u\phi + N_u, \tag{4.6}$$

where L_u and N_u are the linear operator and nonlinear terms, respectively. Equation (4.6) multiplies the complex conjugate of the streamwise velocity, while the conjugate of (4.6) multiplies the streamwise velocity. Similar operations are performed on the wall-normal and spanwise momentum equations. The six equations are then added to obtain the kinetic

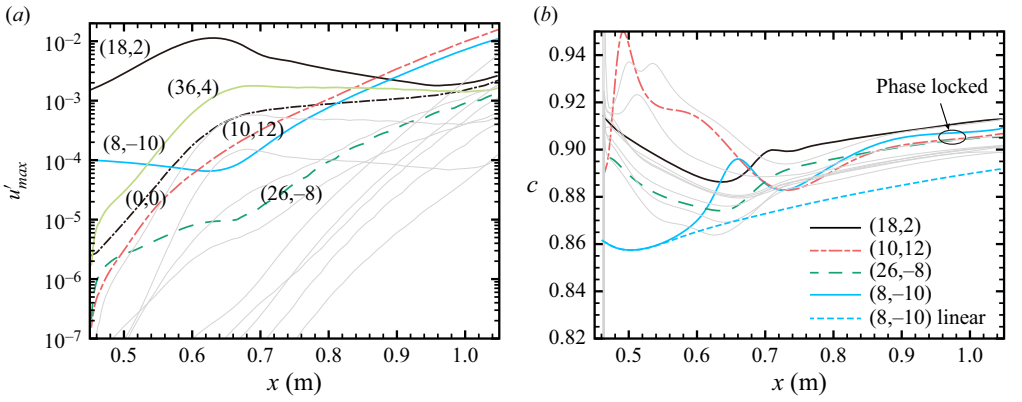

Figure 7. Streamwise evolution of (*a*) the maximum amplitude of the streamwise velocity fluctuation and (*b*) the phase velocity of various modes in the streamwise direction. The higher-harmonic modes are denoted by the grey lines.

energy equation for each mode:

$$\bar{\rho}\frac{\mathrm{D}}{\mathrm{D}t}(|u|^2+|v|^2+|w|^2) = -2\alpha_i\bar{\rho}\bar{U}(|\hat{u}|^2+|\hat{v}|^2+|\hat{w}|^2)\exp\left(-2\int\alpha_i\,\mathrm{d}x\right) = L+N, \tag{4.7}$$

where

$$L = -u^*L_u\phi - v^*L_v\phi - w^*L_w\phi + c.c. \tag{4.8}$$

and

$$N = u^*N_u + v^*N_v + w^*N_w + c.c. \tag{4.9}$$

The linear term L represents the energy transfer between the mode itself and the mean flow. However, the nonlinear term N not only captures the energy transfer between different modes but also includes the energy transfer between the mode itself and the mean flow. The linear transfer can be divided into four parts:

$$L = P + \Xi + \Pi + \upsilon. \tag{4.10}$$

Here, P, Ξ, Π and υ represent the production, energy transfer related to non-parallel terms, pressure dilatation, and diffusion and viscous dissipation, respectively. They are calculated as follows:

$$P = -\bar{\rho}u^*v\frac{\partial\bar{U}}{\partial y} - \bar{\rho}v^*u\frac{\partial\bar{V}}{\partial x} + c.c., \tag{4.11}$$

$$\begin{aligned}\Xi = &-\bar{\rho}u^*u\frac{\partial\bar{U}}{\partial x} + \left(u^*\frac{\partial u}{\partial y} + v^*\frac{\partial v}{\partial y} + w^*\frac{\partial w}{\partial y}\right) - \bar{\rho}v^*v\frac{\partial\bar{V}}{\partial y}\\ &- \rho u^*\left(\bar{U}\frac{\partial\bar{U}}{\partial x} + \bar{V}\frac{\partial\bar{U}}{\partial y}\right) + -\rho v^*\left(\bar{U}\frac{\partial\bar{V}}{\partial x} + \bar{V}\frac{\partial\bar{V}}{\partial y}\right) + c.c.,\end{aligned} \tag{4.12}$$

$$\Pi = -u^*\frac{\partial p}{\partial x} - v^*\frac{\partial p}{\partial y} - w^*\frac{\partial p}{\partial z} + c.c. \tag{4.13}$$

The viscous dissipation and diffusion term is not shown because of its lengthy expression. By integrating (4.7) in the wall-normal direction, the imaginary part of α can be expressed

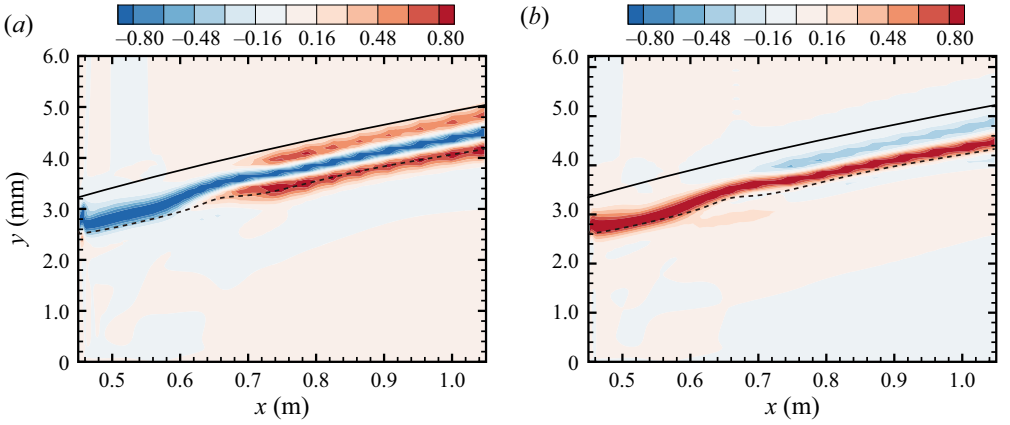

Figure 8. Contours of (*a*) linear and (*b*) nonlinear energy transfer of mode (8,−10). The value is normalized by the maximum value at each streamwise station. The boundary layer and critical layer are denoted by the solid and dashed lines, respectively.

as

$$-\alpha_i = L_\Gamma + N_\Gamma = \int_0^\infty L\,\mathrm{d}y/\boldsymbol{\Gamma} + \int_0^\infty N\,\mathrm{d}y/\boldsymbol{\Gamma}, \tag{4.14}$$

where

$$\boldsymbol{\Gamma} = \int_0^\infty \bar{\rho}\bar{U}(|\hat{u}|^2 + |\hat{v}|^2 + |\hat{w}|^2)\exp\left(-2\int \alpha_i\,\mathrm{d}x\right)\mathrm{d}y. \tag{4.15}$$

Here, L_Γ and N_Γ indicate the growth rates associated with the linear and nonlinear terms, respectively.

The linear and nonlinear energy transfers of mode (8,−10) are depicted in figure 8(*a*,*b*), respectively. As observed, both the linear and nonlinear energy transfers are concentrated around the critical layer. The linear energy transfer is negative from the beginning to the end of the domain and is slightly above the critical layer. Downstream of $x \approx 0.7$ m, the positive linear energy transfer concentrates on the critical layer and is slightly lower than the boundary layer edge. The nonlinear energy transfer is slightly higher than the critical layer and has a negative value downstream of $x \approx 0.7$ m.

To understand the contribution of the linear and nonlinear energy to the evolution of mode (8,−10), the evolution of the integrated linear and nonlinear energy transfer of modes (18,2) and (8,−10) is shown in figure 9(*a*). It is observed that the contribution of nonlinear energy transfer is small for both modes (18,2) and (8,−10), with the change in the amplification rate being primarily due to the linear energy transfer. The linear energy transfer of mode (18,2) is significant at the inlet of the domain, leading to the fast growth of mode (18,2). However, downstream of $x \approx 0.65$ m, the linear energy transfer becomes negative, resulting in a decrease in the amplitude of mode (18,2). Similarly, mode (8,−10) experiences a decrease in its amplitude upstream of $x \approx 0.65$ m due to a negative linear energy transfer. However, downstream of $x \approx 0.65$ m, the significant linear energy transfer results in the rapid growth of mode (8,−10). It can be concluded that mode (18,2) acts as a catalyst, and the rapid growth of mode (8,−10) is directly caused by the energy transfer from the mean flow, which is similar to the conclusions of the study on a flared cone with hypersonic free stream (Chen *et al.* 2017). The linear energy budget of mode (8,−10) shown in figure 9(*b*) reveals that the production term P_Γ plays a major role in the rapid growth of mode (8,−10), with a maximum value of approximately 0.006 at $x \approx 0.7$ m,

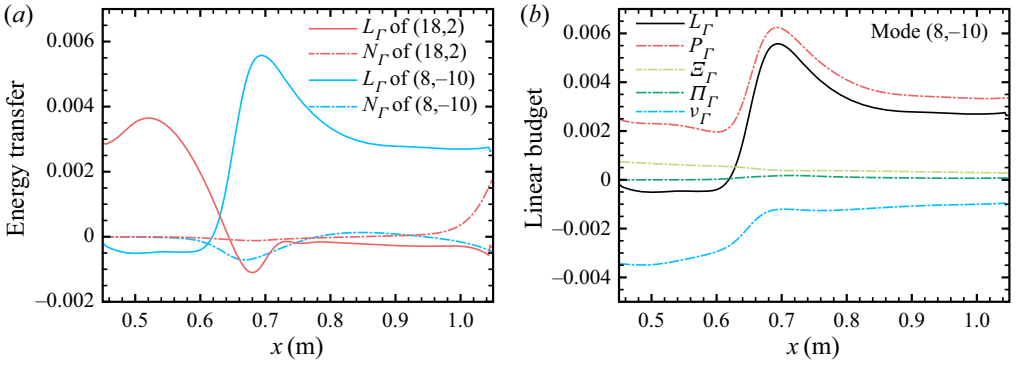

Figure 9. (*a*) Evolution of the integrated linear and nonlinear energy transfer of modes (18,2) and (8,−10); (*b*) linear energy budget of mode (8,−10).

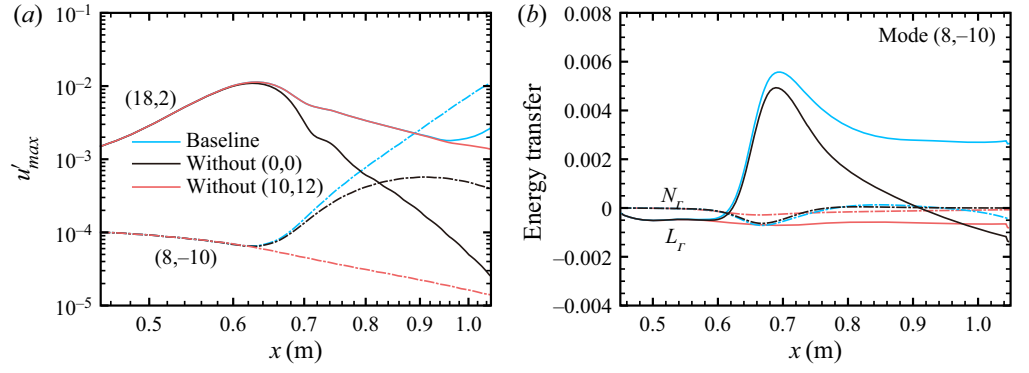

Figure 10. (*a*) Evolution of modes (18,2) and (8,−10) in the streamwise direction; (*b*) evolution of energy transfer of mode (8,−10). Black and red lines indicate that the modes (0,0) and (10,12) are forced to zero in the simulation, respectively.

which is several times larger than the value upstream at $x \approx 0.6$ m. These results indicate that mode (8,−10) gains energy directly from the mean flow, not from mode (18,2).

4.2.2. *Role of the mean-flow distortion and difference mode*

The evolution of modes (18,2) and (8,−10) in a resonant system is shown in figure 10(*a*). The importance of the MFD (0,0) and the difference mode (10,12) is highlighted in this section. When the (0,0) mode is forced to zero, the amplitude of mode (18,2) decreases faster downstream of $x \approx 0.6$ m compared with the baseline. Meanwhile, the amplitude of mode (8,−10) reaches its maximum value at $x \approx 0.9$ m before decreasing. Figure 10(*b*) shows that the maximum value of the linear energy transfer of mode (8,−10) is lower than the baseline and the nonlinear term is less affected. This suggests that the MFD (0,0) plays a role in maintaining the amplitude of mode (18,2), which in turn promotes the growth of the oblique mode (8,10) through linear energy transfer. When the difference mode (10,12) is forced to zero, the amplitude of mode (8,−10) decreases downstream and the rapid growth disappears. The linear energy transfer is negative and the nonlinear energy transfer is close to zero, indicating that the rapid growth is mainly due to the interactions between the second mode (18,2), oblique first mode (8,−10) and difference mode (10,12). Both the second mode (18,2) and the difference mode (10,12) act as catalysts, promoting energy

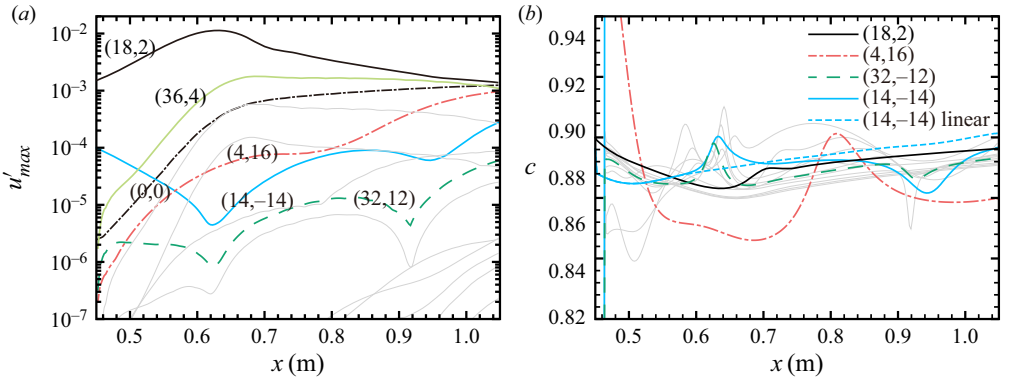

Figure 11. Streamwise evolution of (*a*) the maximum amplitude of the streamwise velocity fluctuation and (*b*) the phase velocity of various modes in the streamwise direction. The higher-harmonic modes are denoted by the grey lines.

transfer from the mean flow to the oblique wave (8,−10). The role of the sum mode is not discussed here owing to its neglected impact in this promotion effect; see figure 18.

4.3. *Interactions between oblique second modes*

In this section, we discuss the interaction between oblique second modes, with mode (14,−14) selected as the representative mode. Fifteen modes are considered in the interaction between modes (18,2) and (14,−14). The evolution of the amplitude and phase velocity of various modes is shown in figure 11. Like the results in figure 6(*a*), mode (14,−14) experiences two rapid growths. However, the promotion effect on the evolution of mode (14,−14) is weaker than the strong promotion effect on the first mode (8,−10). Additionally, there is no phase locking observed between mode (14,−14) and the difference mode (4,16), as seen in figure 11(*b*).

To understand the cause of the rapid growth of mode (14,−14), the contours of linear and nonlinear energy transfer are shown in figure 12. The maximum linear and nonlinear energy transfer is around the critical layer, with linear energy transfer being negative upstream of $x \approx 0.64$ m and positive downstream of $x \approx 0.64$ m. The nonlinear energy transfer is negative from the beginning to the end, with positive values observed at $x \approx 0.7$ m and $x \approx 1.0$ m. The integrated linear and nonlinear energy transfers of modes (18,2) and (14,−14) are shown in figure 13. Unlike for the first mode, where linear energy transfer dominates the energy transfer during the rapid growth, both linear and nonlinear energy transfers are high at $x \approx 0.65$ where the second mode (14,−14) begins to grow rapidly. The nonlinear energy transfer gradually decreases to a negative value as it moves in the streamwise direction and becomes positive downstream of $x \approx 0.95$ where the amplitude of mode (14,−14) increases again. The linear energy transfer is positive downstream of $x \approx 0.65$ and experiences two rapid growths during the rapid growth of mode (14,−14). Hence, the rapid growth of mode (14,−14) is a result of both linear and nonlinear energy transfers. The linear energy transfer comes from the mean flow and mode itself, while the nonlinear transfer can come not only from the mean flow but also from other modes. To address this question, we forced only mode (18,2) at the inlet of NPSE. The energy transfer of mode (18,2) between only the (18,2) initiated and both the modes (18,2) and (14,−14) included coincides with the evolution in the streamwise direction,

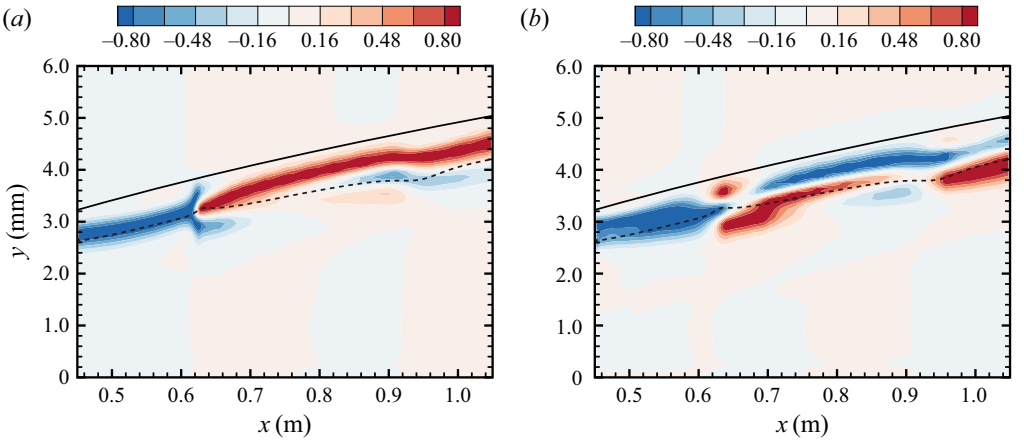

Figure 12. Contours of (*a*) linear and (*b*) nonlinear energy transfer of mode (14,−14). The values are normalized by the maximum value at each streamwise station. The boundary layer and critical layer are denoted by the solid and dashed lines, respectively.

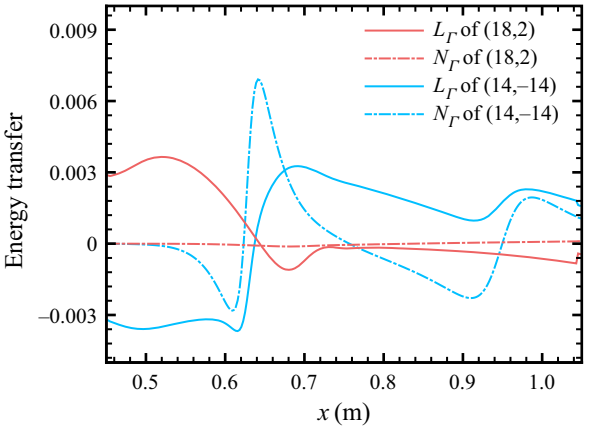

Figure 13. Evolution of the integrated linear and nonlinear energy transfer of modes (18,2) and (14,−14).

as shown in figure 14(*c*). Therefore, the rapid growth of mode (14,−14) is not from mode (18,2), but from the linear energy transfer and mean flow through nonlinear energy transfer.

In the following, the effect of the mean-flow distortion mode (0,0) and difference mode (4,16) will be examined. Modes (0,0) and (4,16) are both forced to zero. The evolution of the maximum amplitudes of modes (18,2) and (4,16) is displayed in figure 14. When mode (0,0) is forced to zero, it can be seen that the mode (18,2) decreases to a lower amplitude compared with the baseline, and the amplitude of mode (14,−14) is also reduced in comparison with the baseline; see figure 14(*a*). Meanwhile, the maximum value of the linear energy transfer is lower than the baseline and is decreasing faster. The maximum value of the nonlinear energy transfer is relatively unaffected; see figure 14(*b*). This suggests that the role of mode (0,0) in interactions between the second modes and between the second mode and the first mode is the same, promoting the increase of the second mode (14,−14) by maintaining the amplitude of mode (18,2). When mode (4,16) is removed, the amplitude of mode (14,−14) steadily decreases until the end of the domain, and the overshoot of both linear and nonlinear energy transfers disappears; see figure 14(*a*,*b*).

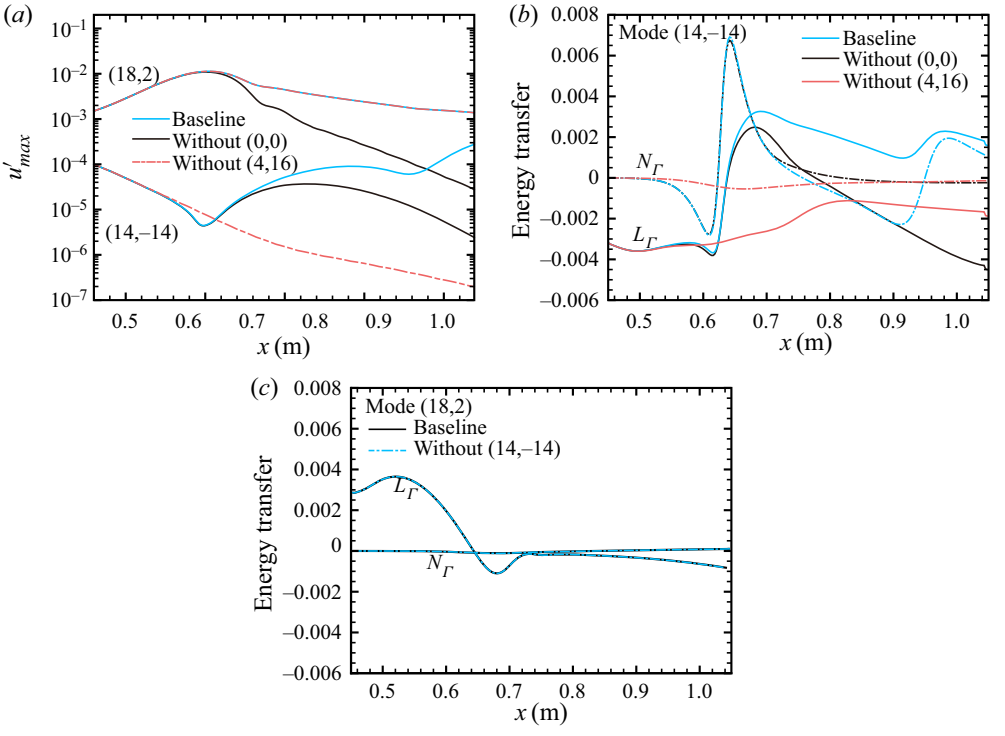

Figure 14. Evolution of (*a*) the amplitudes of modes (18,2) and (14,−14), (*b*) the integrated energy transfer of mode (14,−14), and (*c*) the integrated energy transfer of mode (18,2).

This indicates that the interactions between modes (18,2), (14,−14) and (4,16) are crucial in the rapid growth of mode (14,−14). Both modes (18,2) and (4,16) act as catalysts, facilitating energy transfer from the mean flow to the oblique mode (14,−14).

It is worth noting that, compared with the amplifying effect of the second mode oblique wave on the first mode, the amplifying effect of the second mode oblique wave on the oblique second mode is weaker, and it is difficult for the second mode oblique wave to enter the resonance state with the difference mode it produces.

5. Interaction between a pair of oblique second modes and an oblique wave

In this section, the interactions between a pair of oblique second modes with the same frequency and opposite spanwise wavenumbers and an oblique wave are investigated. The amplitude of each oblique second mode is set at $0.00075u_\infty$, and the sum of the amplitudes of the second mode pair is equal to $0.0015u_\infty$, which is equivalent to the amplitude of a single second mode in § 4. The high amplitude of steady modes will be generated by the interactions between a pair of oblique second modes; thus, the interactions between these steady modes and oblique modes are studied. The simulation involves a total of 25 modes, encompassing both the steady modes and the harmonic modes that result from the interaction between the steady modes and oblique modes.

A parametric study is conducted by considering a pair of second mode oblique waves (18,2) and (18,−2) and another oblique wave at the inlet of the domain. A total of 272 cases are calculated, including 17 frequencies and 16 spanwise wavenumbers. The contours of the nonlinear amplitude and the ratio of nonlinear to linear amplitudes at $x = 1.025$ are

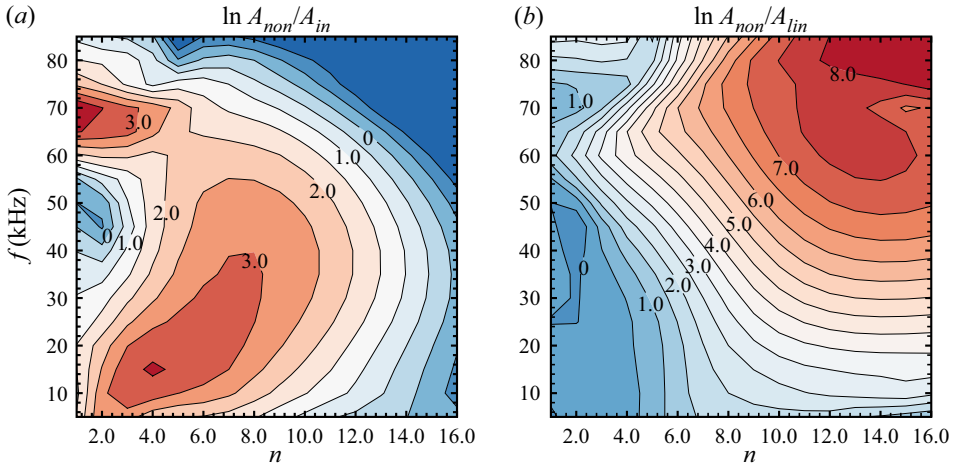

Figure 15. Amplitude of the oblique waves at $x = 1.025$ m: (*a*) contours of the nonlinear amplitude, $\ln A_{non}/A_{in}$; (*b*) contours of the ratio of the nonlinear amplitude to the linear amplitude, $\ln A_{non}/A_{lin}$.

plotted in figure 15. The nonlinear amplitudes of the unstable first and second modes are the highest in the *n*–*f* contours, specifically modes (3,4) and (14,2), as shown in figure 15(*a*). The ratio of nonlinear to linear amplitudes shows that modes with greater spanwise wavenumbers are amplified more, while unstable first and second modes are less amplified; see figure 15(*b*). Overall, the distributions of the nonlinear amplitude and ratio of nonlinear to linear amplitudes are similar to those of the interactions between a single second mode and a single oblique wave. The difference is that the maximum amplitude in figure 15 is lower than that in figure 3. For instance, the maximum value of $\ln A_{non}/A_{in}$ is greater than 5.0 in figure 3(*a*), whereas it is around 3.0 in figure 15(*a*).

The interactions between a pair of oblique second modes and an oblique wave are further studied by selecting mode (8,10) as the representative oblique wave. The evolution of various modes is depicted in figure 16(*a*). A high amplitude of the steady mode (0,4) is observed, which is generated by the interactions between modes (18,−2) and (18,2). Mode (0,8) is generated by interactions between harmonic modes, while modes (10,−8) and (10,−12) are the difference modes and modes (26,8) and (26,12) are the sum modes. The amplitude of mode (8,10) rapidly grows downstream of $x = 0.68$ m, resulting in a phase lock between mode (8,10) and the difference modes; see figure 16(*b*). To investigate the role of various modes, (0,4), (0,8), (0,0), sum modes and difference modes are forced to zero.

The role of different modes on the evolution of oblique wave (8,10) is analysed as shown in figure 17(*a–c*). The high amplitude of mode (0,8) has little effect on the growth of the oblique wave (8,10), as the amplitude of mode (8,10) without mode (0,8) remains almost the same as the baseline case. The linear and nonlinear energy transfer of modes (8,10) and (18,2) is also found to be similar to the baseline. However, when mode (0,0) is forced to zero, the amplitude of mode (18,2) decreased more quickly downstream of $x = 0.63$ m due to reduced linear energy transfer, leading to a decrease in the amplitude of mode (8,10) in the downstream region. Compared with the impact of mode (0,0), the effect of mode (0,4) is weaker on the promotion effect. Overall, the MFD plays a more significant role in promoting the rapid growth of mode (8,10), while the steady modes (0,4) and (0,8) have a limited impact.

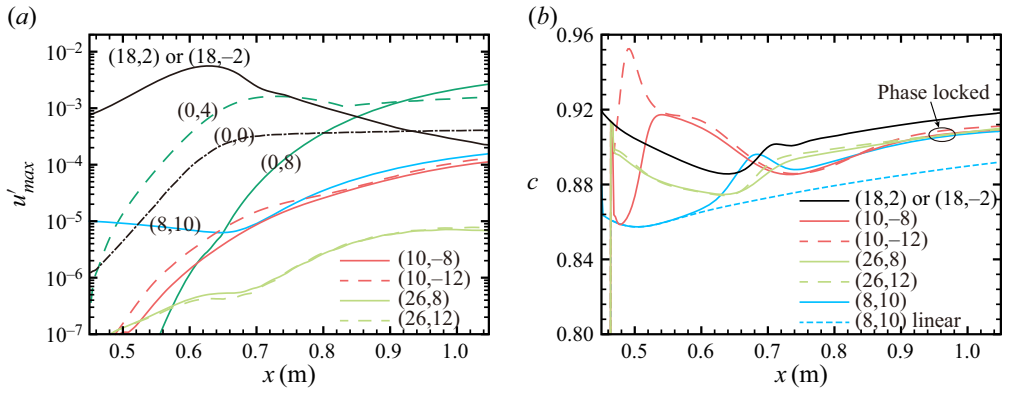

Figure 16. Streamwise evolution of (*a*) the maximum amplitude of the streamwise velocity fluctuation and (*b*) the phase velocity of various modes in the streamwise direction.

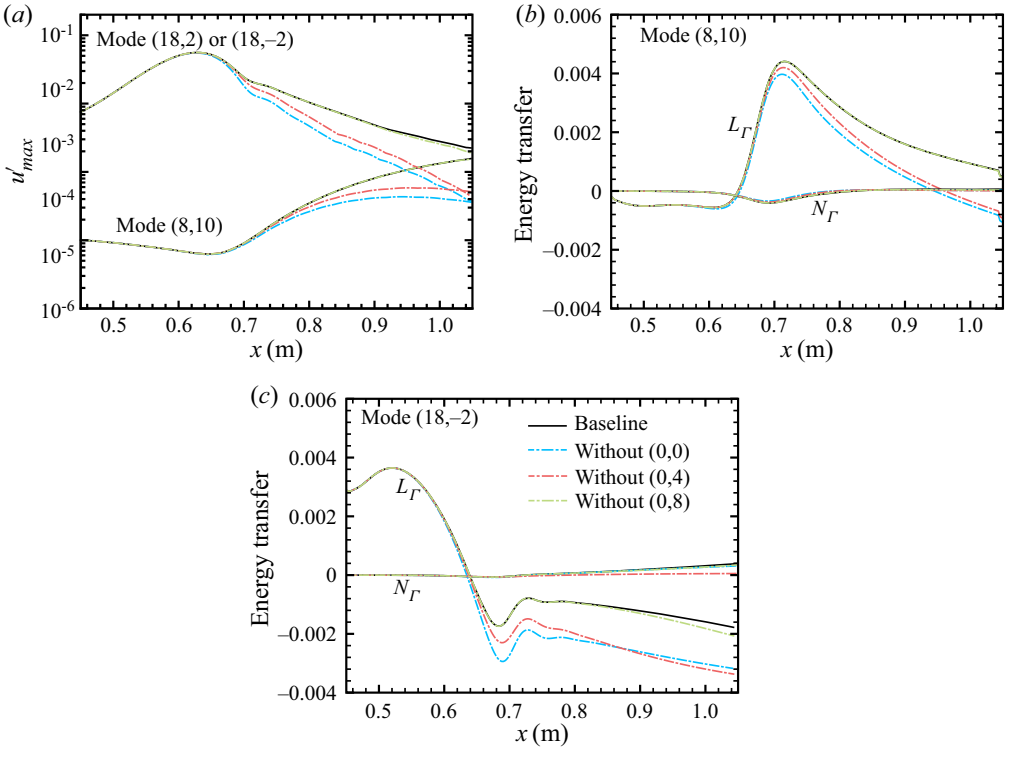

Figure 17. Evolution of (*a*) the amplitude of modes (18,2) and (8,10), (*b*) the energy transfer of mode (8,10) and (*c*) the energy transfer of mode (18,2) in the streamwise direction.

The role of sum and difference modes is also studied, as shown in figure 18. Four cases without modes (10,−8), (10,−12), (26,12) and (26,8) are considered. The results showed that the difference modes (10,−8) and (10,−12) play a crucial role in the fast growth of mode (8,10). When these modes are forced to zero, the amplification of mode (8,10) is not observed. The amplification effect is weaker when only one of the difference modes (10,−8) or (10,−12) is removed. Although phase locking is observed between modes

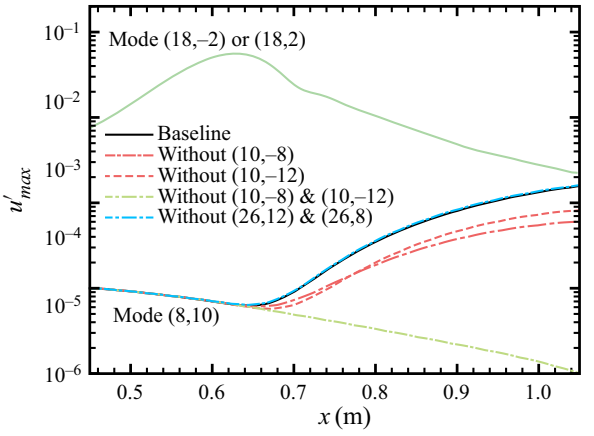

Figure 18. Evolution of the amplitude of modes (18,2) and (8,10), sum modes (26,12) and (26,8), and difference modes (10,−12) and (10,−8) along the streamwise direction.

(8,10) and the sum modes (26,8) and (26,12), the sum modes have negligible effect on the evolution of mode (8,10). When the sum modes are forced to zero, the evolution of mode (8,10) remained almost the same as in the baseline case.

The interactions between a pair of oblique second modes and a single oblique second mode are not shown in this study as the mechanism behind these interactions is similar to the ones discussed in present section and § 4.3.

6. Interaction between a pair of second modes and a pair of oblique waves

The interaction between a pair of oblique second mode waves and a pair of oblique waves is studied using DNS. The use of DNS is necessary as the NPSE have a tendency to diverge and become unreliable in strong nonlinear stages. Furthermore, the aim is to verify two new nonlinear transition paths based on the results above and to thoroughly examine the complete laminar-to-turbulent transition through these two new nonlinear paths using DNS. It is important to note that in this section, (m,n) represents the sum of modes (m,n) and $(m,-n)$ for convenience.

The computational domain for the DNS extends from 0.45 to 1.25 m in the streamwise direction, from 0.0 to 0.1 m in the wall-normal direction and from 0.0 to 0.0375 m in the spanwise direction. The size of the domain normalized by the boundary layer thickness at the inlet is approximately $250.0\delta_{in} \times 25.0\delta_{in} \times 11.7\delta_{in}$. The spanwise width of the domain is equal to the widest spanwise wavelength of the modes in table 2. The grid resolution consists of $2100 \times 175 \times 160$ points in the three dimensions, with a maximum grid resolution of $\Delta x^+_{max} \times \Delta y^+_w \times \Delta z^+_{max} = 10.0 \times 0.5 \times 6.1$ normalized by the maximum wall shear stress τ_w. A similar grid resolution has been validated and used in previous studies (Li *et al.* 2010*a*; Unnikrishnan & Gaitonde 2019). At the inlet of the DNS, an inflow disturbance, obtained from solving the NPSE, is added. This disturbance is expressed as

$$\phi' = \hat{\phi}_{m,n}(x, y) \exp(\mathrm{i}(m\beta z - n\omega t)). \tag{6.1}$$

The mode shapes of modes (18,2), (16,2) and (8,10) are depicted in figure 19, which are normalized by the maximum streamwise velocity fluctuation. Modes (18,2) and (16,2) constitute the oblique second mode, while mode (8,10) belongs to the first oblique mode,

Cases	Inlet modes	Amplitude	$L_x \times L_y \times L_z$ (δ_{in})	$n_x \times n_y \times n_z$
$S1$	(18,2)	0.0032		
$S1_w$	(18,2)	0.0016		
$S2$	(18,2)	0.0016		
	(8,10)	0.00075	$250.0 \times 25.0 \times 11.7$	
$S2$-1	(16,2)	0.0016		$2100 \times 175 \times 160$
	(8,10)	0.00075		
$S3$	(18,2)	0.0008		
	(16,2)	0.0008		
	(8,10)	0.00075		

Table 2. Details of test cases. Here, δ_{in} represents the boundary layer thickness at the inlet.

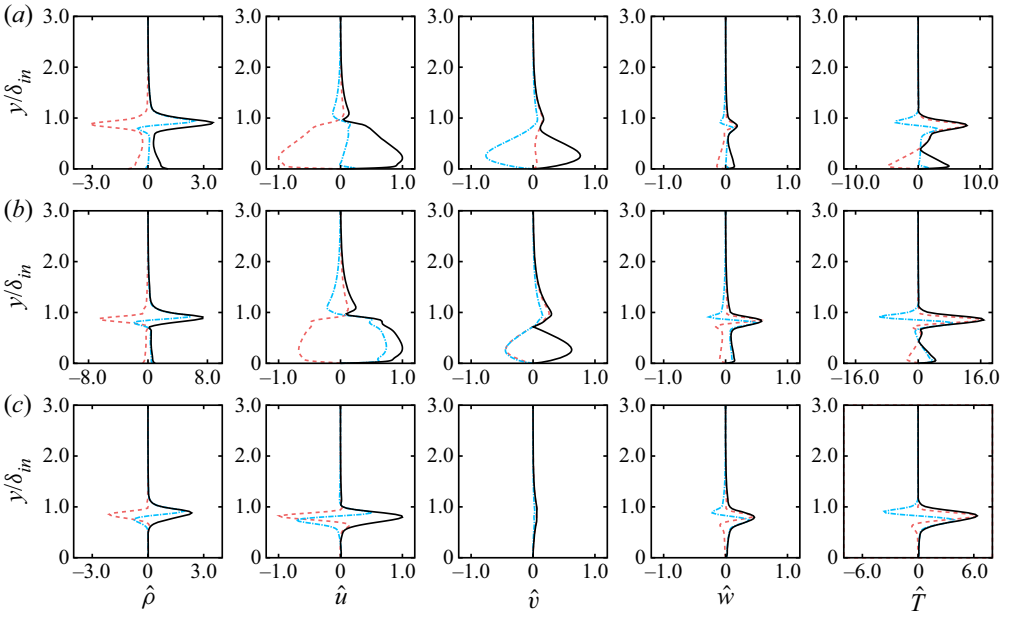

Figure 19. The mode shapes of (*a*) mode (18,2), (*b*) mode (16,2) and (*c*) mode (8,10) at the inlet. The red dashed, blue dash–dotted and solid lines represent the real part, imaginary part and magnitude of the mode shapes, respectively.

as seen in figure 1. The second modes (18,2) and (16,2) exhibit a greater wall-normal disturbance velocity than the first mode (8,10), which is responsible for the lift-up effect and subsequent formation of streaks during the second mode oblique breakdown (Zaki & Durbin 2005, 2006). Additionally, the mode shape of the second modes spans the edge of the boundary layer, whereas that of the first mode is located closer to the edge. These features have important implications for the transition mechanisms in the cases listed in table 2.

6.1. *Nonlinear interactions*

Table 2 presents five cases for study. The reasons for using these five examples will be explained in the following paragraphs.

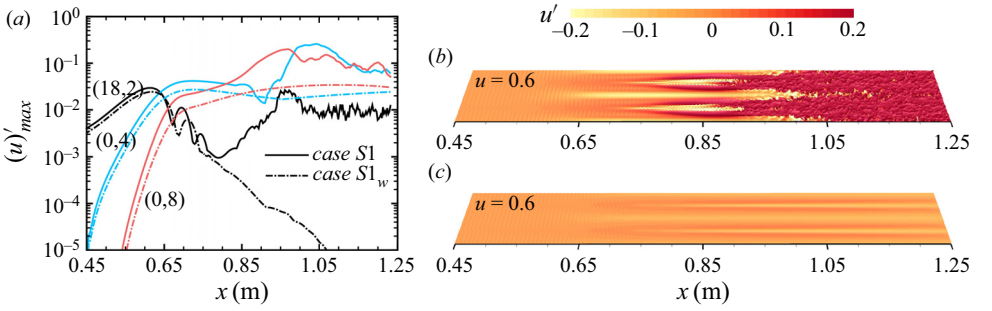

Figure 20. (*a*) Evolution of modes (18,2), (0,4) and (0,8) for cases *S*1 and $S1_w$ in the streamwise direction. Instantaneous iso-surface of streamwise velocity at (*b*) $u = 0.6$ for case *S*1 and (*c*) $u = 0.6$ for case $S1_w$, coloured by the streamwise velocity fluctuations.

The first case, *S*1, is the second mode oblique breakdown, which is initiated by a pair of second mode waves with an initial amplitude of streamwise velocity perturbation of $0.0032u_\infty$. Case $S1_w$ is the second mode oblique breakdown with a weaker initial amplitude of 0.0016 than that of case *S*1. The second mode oblique breakdown has been previously studied in Franko & Lele (2013) and Zhou *et al.* (2022*b*). The nonlinear stage of the second mode oblique breakdown results in the generation of streamwise streaks through the nonlinear interaction of oblique instability waves. These streaks can lead to the self-sustained breakdown of the boundary layer. For instance, the breakdown of streamwise streaks results in the breakdown of the boundary layer in figure 20(*b*). The high amplitude of modes (0,4) and (0,8) in case *S*1 is responsible for the high amplitude of streamwise streaks, as can be seen in figure 20(*a*). However, the self-sustained breakdown of the streaks can only occur when their amplitude reaches a certain threshold value. In case $S1_w$, the amplitude of the steady modes (0,4) and (0,8) is lower than in case *S*1, and the breakdown of streamwise streaks is not observed as in figure 20(*c*). This is because the weaker amplitude of streaks cannot lead to a self-sustaining state of the boundary layer breakdown. However, it is challenging to determine the exact amplitude of streaks that leads to the self-sustaining breakdown of the boundary layer.

6.1.1. *Path 1*

It is interesting to see if the introduction of a damping first oblique mode with low amplitude in case $S1_w$ can trigger transition and result in a fully developed turbulent boundary layer, as a pair of low-amplitude oblique second modes or a pair of low-amplitude oblique first modes with damping amplification alone cannot cause the transition. This hypothesis is tested in case *S*2, which is called path 1 in the present study. In this path, both the second mode (18,2) and the first mode (8,10) are introduced at the inlet of the domain, with initial amplitudes of streamwise velocity disturbance of 0.0016 and 0.00075, respectively. The goal is to determine if this new transition path leads to a self-sustaining state of the breakdown of the boundary layer and if it results in a fully developed turbulent boundary layer. The results of case *S*2 will provide insights into the effect of combining the oblique second mode and a damping first oblique mode on the transition mechanism.

The breakdown of the boundary layer can be seen from figure 21(*b–e*). To determine the cause of the boundary layer breakdown, the evolution of the modes in the streamwise direction for case *S*2 is shown in figure 21(*a*). It is observed that the amplitude of

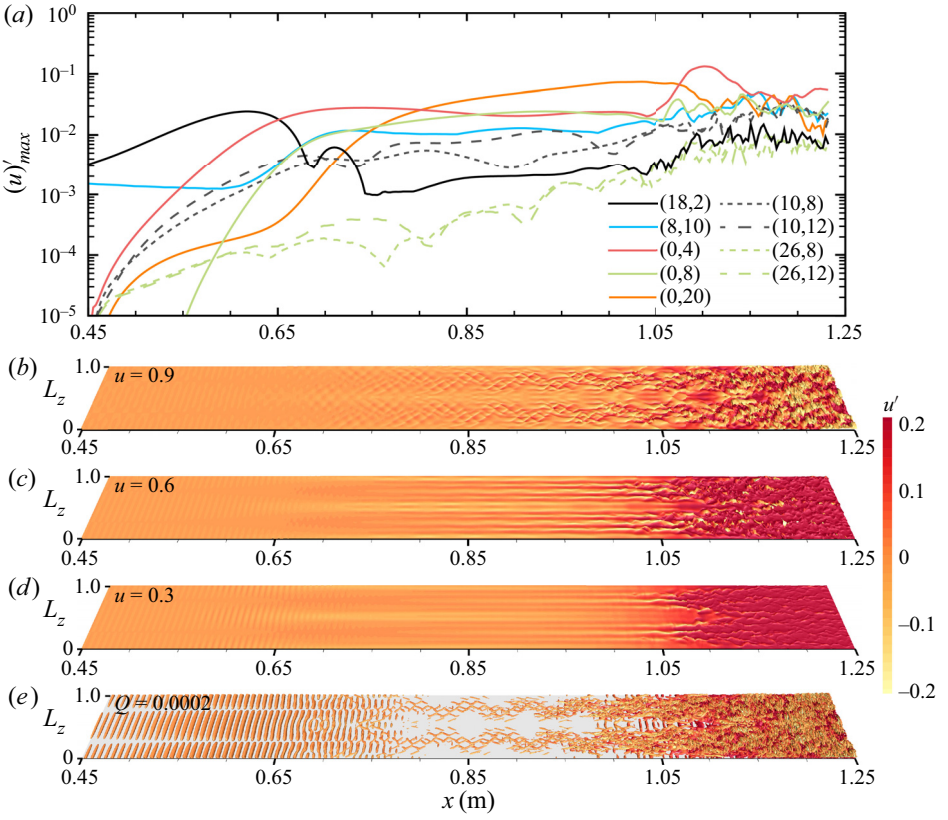

Figure 21. (*a*) The evolution of various modes for case *S*2 in the streamwise direction. The instantaneous iso-surfaces of the streamwise velocity for (*b*) $u = 0.9$, (*c*) $u = 0.6$ and (*d*) $u = 0.3$. (*e*) Instantaneous iso-surface of $Q = 0.0002$ for case *S*2, coloured by the streamwise velocity fluctuations.

mode (8,10) decreases upstream of $x \approx 0.6$ m and then rapidly grows downstream of this streamwise station. This observation is consistent with the results of NPSE, which found that the oblique second mode leads to the rapid growth of the first oblique modes. Moreover, the interaction between modes (8,10) and (18,2) results in the generation of difference modes (10,8) and (10,12) and sum modes (26,8) and (26,12). The amplitude of difference modes is approximately one order of magnitude higher than that of sum modes.

The evolution of oblique waves (18,2) and (8,10) can be visualized using the *Q*-criterion as shown in figure 21(*e*). The oblique wave induced by mode (18,2) dominates the flow field upstream of $x \approx 0.75$. As the amplitude of mode (18,2) decreases, this oblique wave disappears. Subsequently, a second type of oblique wave in the form of Λ shapes is observed due to the high amplitude of mode (8,10). Although the amplitude of mode (8,10) grows to a high level, it is still lower than the amplitudes of modes (0,4) and (0,8), which are generated by the nonlinear interactions of mode (18,2). Due to the high amplitude of mode (8,10), the interaction between the oblique wave and streaks causes a weak distortion of the streaks from $x \approx 0.7$ to $x \approx 0.8$ m; see figure 21(*c*,*d*). However, this distortion is not enough to cause the breakdown of the boundary layer. The evolution of modes (0,4) and (0,8) between cases $S1_w$ and *S*2 is almost the same upstream of $x \approx 1.0$ m where the boundary layer is about to break down in case *S*2, as shown in figures 22 and 21. This indicates that the rapid growth of mode (8,10) has limited effect on the

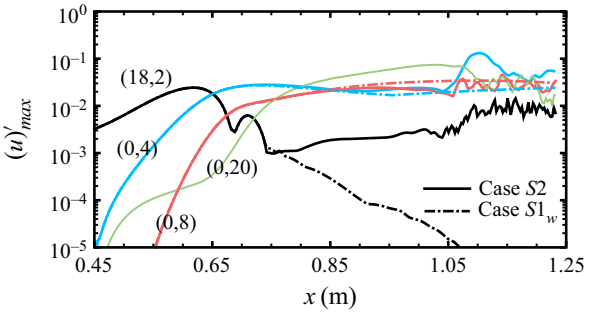

Figure 22. Evolution of modes (18,2), (0,4), (0,8) and (0,20) in the streamwise direction for cases $S2$ and $S1_w$.

steady modes (0,4) and (0,8) generated during the nonlinear interactions of the second mode oblique breakdown. The interactions between oblique waves and streaks generated by the oblique second mode are relatively weak; however, the interactions between modes (8,10) and (0,20) are quite strong. These nonlinear interactions between modes (8,10) cause the high amplitude of mode (0,20) in figure 21(a) from approximately $x = 0.8$ to $x = 1.0$ m, which is even higher than for modes (0,4) and (0,8). As a result, the high amplitude of mode (0,20) leads to high-amplitude streaks with smaller scale in the spanwise direction, as seen in figure 21(c,d). The strong interaction between the oblique wave and these streaks results in significant distortion of the streaks from approximately $x = 0.8$ to $x = 1.0$ m, which eventually leads to the breakup of streaks at $x = 1.0$ m, as shown in figure 21(c,d). The breakdown of the Λ-shaped structure occurs slightly upstream of $x = 0.95$ m compared with the streaks, as seen in figure 21(c,e).

6.1.2. *Path 2*

As mentioned above, the oblique second mode has a promotion effect on the oblique first mode. In addition, the unstable region of the second mode with lower frequency is more downstream than that of the second mode with higher frequency. Based on these two results, the addition of the oblique second mode (16,2) into case $S2$ results in the formation of case $S3$. The aim of this set-up is twofold: first, to investigate if the transition to turbulence can occur with a second mode of lower initial amplitude than in case $S2$. Second, to verify that the oblique mode (8,10) can be promoted by the two oblique second modes (18,2) and (16,2) at two different streamwise locations, creating a domino-like effect. To achieve these objectives, the modes (18,2), (16,2) and (8,10) are added at the inlet of case $S3$ with initial amplitudes of streamwise velocity perturbation of $0.0008u_\infty$, $0.0008u_\infty$ and $0.00075u_\infty$, respectively. Thus, case $S3$ represents path 2.

The evolution of modes, including the instantaneous iso-surface of the streamwise velocity and the iso-surface of the Q-criterion, are depicted in figure 23. As shown in figure 23(d), the boundary layer breaks down into smaller scales. Furthermore, compared with case $S2$, the breakup station of the boundary layer in case $S3$ occurs upstream. The reason behind the early boundary layer breakdown can be found in the evolution of various modes; see figure 23(a). The amplitude of mode (8,10) experiences a twofold increase, with the first beginning at $x \approx 0.6$ m, due to the promotion effect of mode (18,2), and the second beginning at $x \approx 0.8$ m, due to mode (16,2). As a result of the first promotion, the amplitude of mode (8,10) increases to a high level, leading to stronger interactions between modes (16,2) and (8,10) than between modes (18,2) and (8,10). For example, the amplitude of the difference modes (8,8) and (8,12) generated by the interactions between modes

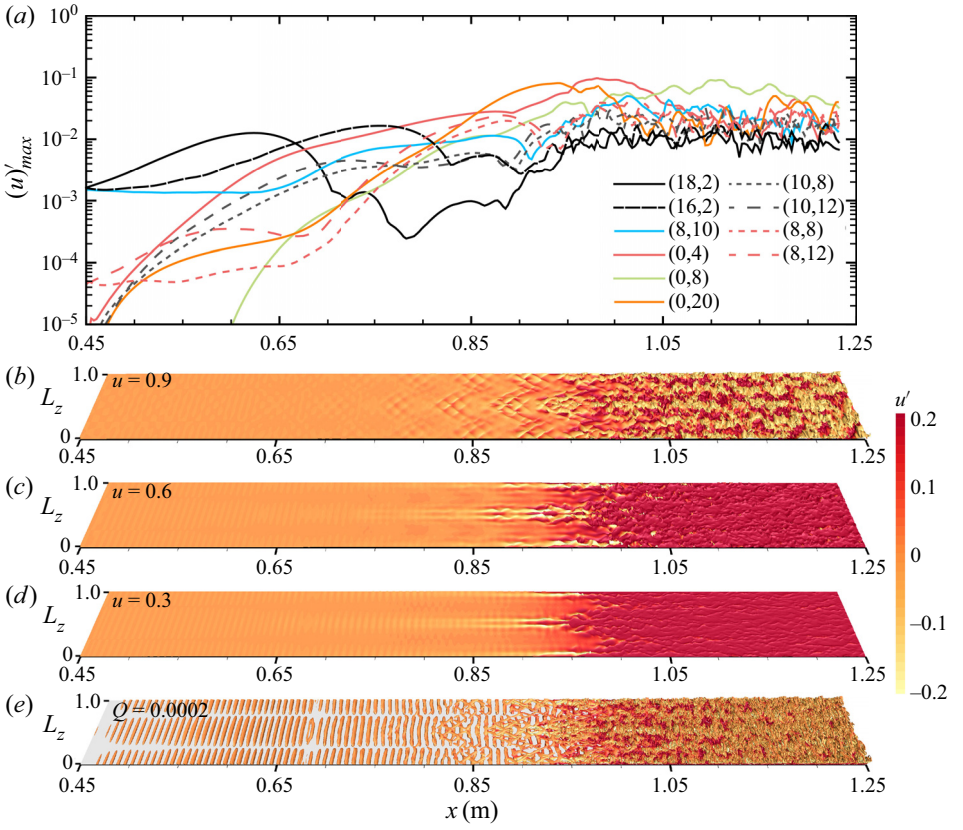

Figure 23. (*a*) The evolution of various modes for case *S*3 in the streamwise direction. The instantaneous iso-surfaces of the streamwise velocity for (*b*) $u = 0.9$, (*c*) $u = 0.6$ and (*d*) $u = 0.3$. (*e*) Instantaneous iso-surface of $Q = 0.0002$ for case *S*3, coloured by the streamwise velocity fluctuations.

(16,2) and (8,10) is higher than that of the difference modes (10,8) and (10,12) generated by modes (18,2) and (8,10), which is almost the same as that of the steady modes (0,4) at $x \approx 0.87$ m. The two-stage promotion process on mode (8,10) results in a high amplitude of mode (0,20), leading to the boundary layer transition due to the high amplitude of oblique modes, difference modes and steady modes. In the flow field structure, the breakdown of streaks and Λ-shaped vortices leads to the breakdown of the boundary layer, which is in agreement with the modal results; see figure 23(*c*,*e*).

In order to elucidate the specific roles played by modes (16,2) and (18,2) in the two-stage promotion processes, case *S*2-1 is employed as an illustrative example. The inlet disturbances consist of modes (16,2) and (8,10) with respective amplitudes of 0.0016 and 0.00075. The results pertaining to mode (8,10) for cases *S*2, *S*2-1 and *S*3 are depicted in figure 24. It is observed that both modes (18,2) and (16,2) can induce significant amplification of mode (8,10). In the case of *S*2-1, the rapid growth of mode (8,10) commences at $x \approx 0.75$ m, while in case *S*2 it initiates at $x \approx 0.6$ m. Notably, these two positions align with the locations where the two-stage promotion of mode (8,10) begins in case S3. Consequently, the two-stage promotion of mode (8,10) in case *S*3 can be attributed to modes (18,2) and (16,2).

In conclusion, the realization of path 1 by case *S*2 demonstrates that a pair of low-amplitude second oblique waves alone cannot lead to the second mode

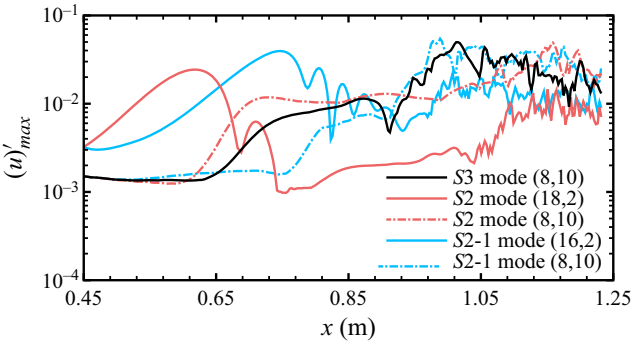

Figure 24. Evolution of modes (18,2) and (8,10) for case *S*2, modes (16,2) and (8,10) for case *S*2-1, and mode (8,10) for case *S*3 in the streamwise direction.

oblique breakdown. However, the addition of a pair of low-amplitude damping first oblique modes does lead to the breakup of the boundary layer. This suggests that the transition cannot be achieved by either of these two types of disturbances alone, but only through their combination. Case *S*3 is an example of path 2 and demonstrates that a combination of three low-amplitude modes can trigger a domino-like process, resulting in the rapid breakdown of the boundary layer with a lower initial amplitude of the second mode than in case *S*2.

6.2. *Turbulent region*

In the end, our goal is to determine if either of the two transition paths can lead to a fully developed turbulent boundary layer. At a fully developed turbulent boundary layer, the skin-friction coefficient and heat transfer on the wall can be described by theoretical correlations as documented in White (2006). The adiabatic wall temperature T_{aw} is calculated using an approximation presented in White (2006),

$$T_{aw} = T_\infty \left(1 + r\frac{\gamma - 1}{2} Ma_\infty^2\right), \tag{6.2}$$

where $r = Pr^{1/3}$. The turbulent correlation of the skin-friction coefficient, as presented in White (2006) and Bradshaw (1977), has been validated for the case of a non-adiabatic wall and is used in this study:

$$C_f = \frac{0.455}{S}\left[\ln\left(\frac{0.06}{S}(Re_x - Re_{x_{in}})\frac{\mu_\infty}{\mu_w}\sqrt{\frac{T_\infty}{T_w}}\right)\right]^{-2}, \tag{6.3}$$

where

$$S = \frac{\sqrt{(T_{aw}/T_\infty - 1)}}{\arcsin(A) + \arcsin(B)}. \tag{6.4}$$

The subscripts ∞ and w denote the conditions at the free stream and wall, respectively. The parameters A and B are defined as

$$A = \frac{2a^2 - b}{\sqrt{b^2 + 4a^2}}, \quad B = \frac{b}{\sqrt{b^2 + 4a^2}} \tag{6.5a,b}$$

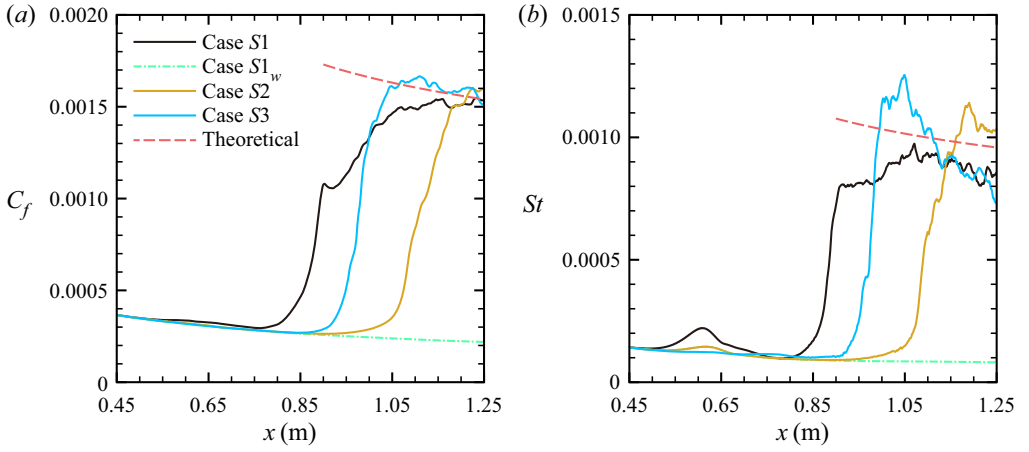

Figure 25. Evolution of (*a*) the skin-friction coefficient C_f and (*b*) the Stanton number St for cases $S1$, $S1_w$, $S2$ and $S3$.

where

$$a = \sqrt{r\frac{\gamma - 1.0}{2}Ma_\infty^2\frac{T_\infty}{T_w}}, \quad b = \left(\frac{T_{aw}}{T_w} - 1\right). \tag{6.6a,b}$$

Based on the Reynolds analogy (White 2006), the Stanton number is

$$St = \frac{C_f}{2Pr^{2/3}}. \tag{6.7}$$

The evolution of the skin-friction coefficient C_f and Stanton number St is plotted in figure 25. Owing to the high initial amplitude of the second mode, the transition onset in case $S1$ is earlier than in other cases. And the skin friction shows good agreement between the computational and theoretical results at the end of the domain. The skin friction of case $S1_w$ stays at the laminar value. Case $S3$ exhibits the most developed turbulent boundary layer owing to its rapid and early transition, with skin-friction values consistently aligning with theoretical values from $x \approx 1.05$ m. In contrast, case $S2$ exhibits a very short turbulent region due to its late transition and skin-friction values that align with theoretical values over a shorter range. The Stanton number shows an overshoot in heat transfer for cases $S2$ and $S3$ in the transition region, with case $S2$ failing to recover its value to the turbulent value due to the limited length of the computational domain. The DNS values of the Stanton number for both cases $S1$ and $S3$ are lower than the theoretical values. An additional overshoot in heat transfer is also observed in the laminar region for cases $S2$ and $S1$, with case $S1$ exhibiting a greater overshoot due to the higher initial amplitude of the second mode. The additional heat transfer overshoot is caused by the dilatation dissipation generated by the saturated oblique second mode, as reported in works such as Zhu *et al.* (2018) and Zhou *et al.* (2022*b*). It should be noted that the additional heat transfer overshoot in the laminar region vanishes in case $S3$ due to the low initial amplitudes of the second modes (18,2) and (16,2), which cannot lead to strong dilatation dissipation.

Finally, the mean-flow scaling transformation is utilized to examine the development of the mean streamwise profile, moving from the laminar to the turbulent boundary layer. Two transformation methods, namely the Van Driest transformation (Van Driest 1951) and the total-stress-based transformation proposed by Griffin *et al.* (2021), are

employed in this study. In comparison with the Van Driest transformation, the mean-flow transformation introduced by Griffin *et al.* (2021) demonstrates broader applicability, particularly for walls experiencing heat transfer. For the Van Driest transformation, the streamwise velocity and length are normalized based on the friction velocity and the length scale at the wall, respectively. They are defined as

$$U_{VD}^{+} = \frac{U_{VD}}{u_\tau} \tag{6.8}$$

and

$$y^{+} = \frac{\rho_w u_\tau y}{\mu_w}, \tag{6.9}$$

respectively, where the friction velocity is calculated as

$$u_\tau = \sqrt{\frac{\tau_w}{\rho_w}}. \tag{6.10}$$

The Van Driest transform is in form of

$$U_{VD} = \int_0^u \sqrt{\frac{\rho}{\rho_w}}\,\mathrm{d}u. \tag{6.11}$$

For the total-stress-based transformation of Griffin *et al.* (2021), a semilocal wall-normal coordinate is used, which is calculated as

$$Y^{+} = \frac{y\sqrt{\tau_w \rho}}{\mu}. \tag{6.12}$$

The form of the transformation is

$$U^{+} = \int_0^{Y^{+}} S_\tau^{+}\,\mathrm{d}Y^{+}. \tag{6.13}$$

The details of the generalized non-dimensional mean shear S_τ^{+} can be found in Griffin *et al.* (2021). The scaled mean streamwise velocity for cases *S*2 and *S*3 is shown in figure 26. In the turbulent region, the scaled mean profile should match the theoretical formulas

$$U_{VD}^{+} = y^{+} \quad \text{and} \quad U_{VD}^{+} = 2.5\ln y^{+} + 5.5, \tag{6.14a,b}$$

at the viscous sublayer and the log layer (Coles 1956), respectively.

The simulation results demonstrate that the mean streamwise velocity profile, when scaled using the approach proposed by Griffin *et al.* (2021), progressively approaches the theoretical value as it evolves in the streamwise direction for cases *S*2 and *S*3, particularly within the log layer at $x = 1.225$ m; see figure 26(*b*,*d*). In addition, the theoretical results closely align with the results obtained from the Van Driest transformation at $x = 1.225$ m for cases *S*2 and *S*3; see figure 26(*a*,*c*). However, a slight disparity is observed in the slope rate of the scaled velocity between the theoretical values and those obtained using the Van Driest transformation. Notably, a similar difference was reported in a previous study by Guo *et al.* (2022). Overall, the results of the skin-friction distribution and the scaled mean streamwise velocity provide evidence that these two new transition paths can lead to a fully developed boundary layer.

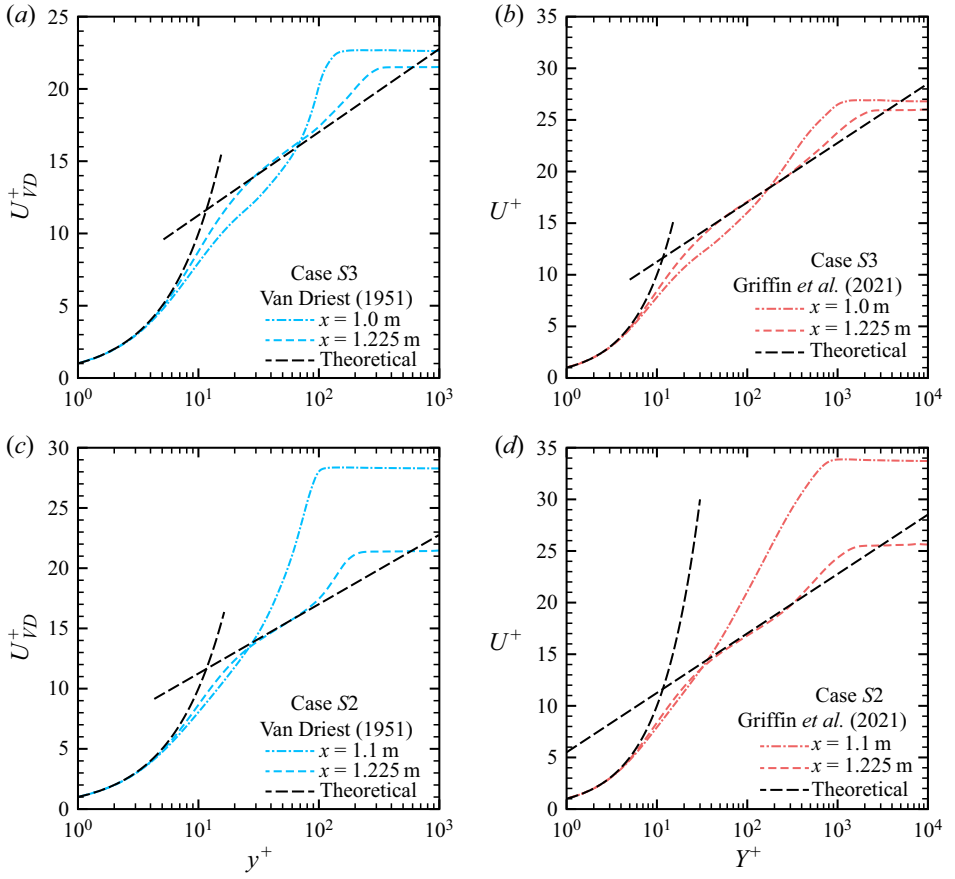

Figure 26. Evolution of the scaled mean streamwise velocity at different streamwise stations for (*c*,*d*) case *S*2 and (*a*,*b*) case *S*3. The blue and red lines are results scaled by the Van Driest transformation (Van Driest 1951) and total-stress-based transformation of Griffin, Fu & Moin (2021), respectively.

7. Conclusions

The nonlinear interactions between oblique second mode and oblique waves in a high-speed boundary layer at Mach 4.5 are investigated using a combination of LST, NPSE and DNS.

The results of the LST reveal the presence of first and second mode instabilities in the boundary layer. Further parametric analysis of the interactions between oblique waves using NPSE shows that the presence of an oblique second mode can enhance a broad range of oblique waves, including both first and second modes. The low-amplitude oblique waves with a small spanwise wavenumber have been found to be less amplified by the oblique second mode. However, as the spanwise wavenumber of the oblique wave increases, the rate of amplification predicted by NPSE becomes greater compared with the linear results. Despite this, the linear amplification rate of oblique waves with larger spanwise wavenumbers is more damping. As a result, the oblique wave with the greatest nonlinear amplification may not necessarily be the most amplified wave when considering both linear and nonlinear amplification. The frequency of the most amplified oblique waves is around 40 kHz, and the wave angle between the oblique second mode and the oblique wave is approximately 50°. The interaction between the rapidly growing second mode

and the oblique modes results in the formation of a difference mode, and the parametric resonance between the difference mode and the oblique waves is the key factor driving the amplification effect. Mean-flow distortions (0,0) also play a beneficial role in amplifying the oblique waves. Kinetic energy transfer shows that the oblique wave gains energy from the mean flow, not the oblique second mode. The results of parametric and kinetic energy transfer studies suggest that the mechanisms and outcomes of the interactions between a pair of oblique second modes and a single oblique wave are similar to those between a single second mode and an oblique wave, as the steady modes generated by a pair of oblique second modes have a limited impact on the oblique wave.

Based on the results of the NPSE study, we propose two transition paths that have been analysed using DNS. The first path involves the combination of a pair of low-amplitude oblique second modes and a pair of low-amplitude oblique first modes with damping amplification. It is important to note that a pair of low-amplitude oblique second modes or a pair of low-amplitude oblique first modes with damping amplification alone cannot cause the transition. It leads to the transition of the boundary layer, as the amplified effect of the second mode on the first mode causes a high amplitude of the oblique first mode. Then, the interaction between a pair of high-amplitude oblique first modes results in a high-amplitude steady mode. The breakup of the oblique first mode and this steady mode results in the boundary layer breakdown. The second path involves the combination of different types of oblique waves with appropriate parameters, which leads to a domino-like effect and the rapid breakup of the boundary layer, even with a lower initial amplitude than for the first path. Our DNS analysis has identified the domino-like process, where two oblique second modes cause oblique first modes to be amplified at two different streamwise stations, leading to a rapid breakdown of the boundary layer. Finally, our DNS results show that both of these transition mechanisms can lead to a fully developed turbulent boundary layer.

Acknowledgements. The authors would like to acknowledge Professor X. Li (Institute of Mechanics, Chinese Academy of Sciences) for the DNS code OpenCFD.

Funding. This study was supported by grants from the National Natural Science Foundation of China (grant no. 92252201) and the Academic Excellence Foundation of BUAA for PhD Students.

Declaration of interests. The authors report no conflict of interest.

Author ORCIDs.
Teng Zhou https://orcid.org/0000-0002-8288-6188;
Zaijie Liu https://orcid.org/0000-0002-1540-6666;
Yuhan Lu https://orcid.org/0000-0002-6276-0385;
Chao Yan https://orcid.org/0000-0002-2691-7955.

Appendix. Validation of solvers

To validate the DNS and NPSE solver used in the current study, simulations of the second mode oblique breakdown are conducted using both DNS and NPSE. The free-stream conditions are the same as those listed in table 1. A pair of oblique second modes, (18,2) and (18,−2), with an amplitude of $0.001u_\infty$ of the streamwise velocity fluctuation, is seeded at the inlet located at $x_0 = 0.45$ m. As shown in figure 27(*a*), there is good agreement between the results obtained from DNS and NPSE. In addition, the results from our NPSE solver agree well with those reported in Chang & Malik (1994), which can be found in our previous study (Zhou *et al.* 2023).

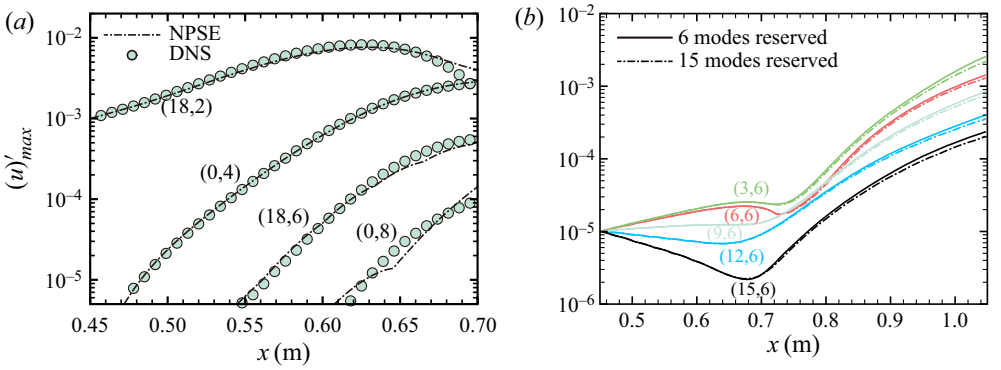

Figure 27. (*a*) Comparison of the evolution of modes in a Mach 4.5 boundary layer solved by the NPSE and DNS methods used in the present study. (*b*) The evolution of five modes involved in the interactions with a single second mode for cases of six modes and fifteen modes reserved.

Finally, the accuracy of considering only six modes to capture the interactions between a single second mode and an oblique wave in § 4 is validated by comparing it with the case where fifteen modes are included. As mentioned earlier, the fifteen modes include the six modes along with their higher-harmonic modes. The initial amplitude of the oblique second mode (18,2) is $0.0015u_\infty$, and is $10^{-5}u_\infty$ for the five oblique waves. The evolution of five modes interacting with the single mode (18,2) separately is depicted in figure 27(*b*). It is evident that the nonlinear evolution of the different modes obtained from the six-mode and fifteen-mode cases exhibits good agreement. This agreement confirms the reliability of the DNS and NPSE solvers employed in this study. Thus, the utilization of the six reserved modes in the computation is considered accurate. The validation of the LST solver can be found in Zhou *et al.* (2022*a*).

References

Adams, N.A. & Kleiser, L. 1996 Subharmonic transition to turbulence in a flat-plate boundary layer at Mach number 4.5. *J. Fluid Mech.* **317**, 301–335.

Al-Salman, A. 2003 Nonlinear modal interactions in a compressible boundary layer. PhD thesis, Imperial College London.

Bradshaw, P. 1977 Efficient implementation of weighted ENO schemes. *Annu. Rev. Fluid Mech.* **9**, 33.

Chang, C.-L. 2004 Langley stability and transition analysis code (LASTRAC) version 1.2 user manual. *Tech. Rep.* NASA/TM-2004-213233. NASA Langley Research Center.

Chang, C.-L. & Malik, M.R. 1994 Oblique-mode breakdown and secondary instability in supersonic boundary layers. *J. Fluid Mech.* **273**, 323–360.

Chen, X., Zhu, Y. & Lee, C. 2017 Interactions between second mode and low-frequency waves in a hypersonic boundary layer. *J. Fluid Mech.* **820**, 693–735.

Coles, D. 1956 The law of the wake in the turbulent boundary layer. *J. Fluid Mech.* **1** (2), 191–226.

Craig, S.A., Humble, R.A., Hofferth, J.W. & Saric, W.S. 2019 Nonlinear behaviour of the Mack mode in a hypersonic boundary layer. *J. Fluid Mech.* **872**, 74–99.

Fasel, H.F., Thumm, A. & Bestek, H. 1993 Direct numerical simulation of transition in supersonic boundary layers: oblique breakdown. In *Fluids Engineering Conference*, p. 77. ASME.

Fedorov, A.V. 2003 Receptivity of a high-speed boundary layer to acoustic disturbances. *J. Fluid Mech.* **491**, 101–129.

Fedorov, A.V., Ryzhov, A.A., Soudakov, V.G. & Utyuzhnikov, S.V. 2013 Receptivity of a high-speed boundary layer to temperature spottiness. *J. Fluid Mech.* **722**, 533–553.

Franko, K.J. & Lele, S.K. 2013 Breakdown mechanisms and heat transfer overshoot in hypersonic zero pressure gradient boundary layers. *J. Fluid Mech.* **730**, 491–532.

FRANKO, K.J. & LELE, S. 2014 Effect of adverse pressure gradient on high speed boundary layer transition. *Phys. Fluids* **26** (2), 024106.

GÖRTLER, H. 1954 *On the Three-Dimensional Instability of Laminar Boundary Layers on Concave Walls*, vol. 1375. National Advisory Commitee for Aeronautics.

GRIFFIN, K.P., FU, L. & MOIN, P. 2021 Velocity transformation for compressible wall-bounded turbulent flows with and without heat transfer. *Proc. Natl Acad. Sci. USA* **118** (34), e2111144118.

GUO, P., SHI, F., GAO, Z., JIANG, C., LEE, C.-H. & WEN, C. 2022 Heat transfer and behavior of the Reynolds stress in Mach 6 boundary layer transition induced by first-mode oblique waves. *Phys. Fluids* **34** (10), 104116.

HADER, C. & FASEL, H.F. 2019 Direct numerical simulations of hypersonic boundary-layer transition for a flared cone: fundamental breakdown. *J. Fluid Mech.* **869**, 341–384.

HAJJ, M.R., MIKSAD, R.W. & POWERS, E.J. 1993 Fundamental–subharmonic interaction: effect of phase relation. *J. Fluid Mech.* **256**, 403–426.

HARTMAN, A.B., HADER, C. & FASEL, H.F. 2021 Nonlinear transition mechanism on a blunt cone at Mach 6: oblique breakdown. *J. Fluid Mech.* **915**, R2.

HARVEY, W.D. 1978 Influence of free-stream disturbances on boundary-layer transition. *NASA Tech. Memorandum* 78635. National Aeronautics and Space Administration Scientific and Technical Information Office.

HERBERT, T. 1988 Secondary instability of boundary layers. *Annu. Rev. Fluid Mech.* **20** (1), 487–526.

HUSMEIER, F. & FASEL, H.F. 2007 Numerical investigations of hypersonic boundary layer transition for circular cones. In *18th AIAA Computational Fluid Dynamics Conference*, p. 289. American Institute of Aeronautics and Astronautics.

JAHANBAKHSHI, R. & ZAKI, T.A. 2019 Nonlinearly most dangerous disturbance for high-speed boundary-layer transition. *J. Fluid Mech.* **876**, 87–121.

JIANG, G.S. & SHU, C.W. 1996 Efficient implementation of weighted ENO schemes. *J. Comput. Phys.* **126** (1), 202.

KACHANOV, Y.S. 1994 Physical mechanisms of laminar-boundary-layer transition. *Annu. Rev. Fluid Mech.* **26** (1), 411–482.

LEINEMANN, M., HADER, C. & FASEL, H.F. 2020 Direct numerical simulations of the nonlinear transition regime on a flat plate at Mach 6. In *AIAA Scitech 2020 Forum*, p. 0586. American Institute of Aeronautics and Astronautics.

LEINEMANN, M., HADER, C. & FASEL, H.F. 2021 Direct numerical simulations of the nonlinear boundary layer transition regime on a flat plate at Mach 6. In *AIAA Scitech 2021 Forum*, p. 1739. American Institute of Aeronautics and Astronautics.

LI, X., TONG, F.-L., YU, C.-P. & LI, X.-L. 2019 Statistical analysis of temperature distribution on vortex surfaces in hypersonic turbulent boundary layer. *Phys. Fluids* **31** (10), 106101.

LI, X.-L., FU, D.-X. & MA, Y. 2010*a* Direct numerical simulation of hypersonic boundary layer transition over a blunt cone with a small angle of attack. *Phys. Fluids* **22** (2), 025105.

LI, X.-L., FU, D.-X., MA, Y.-W. & LIANG, X. 2010*b* Development of high accuracy CFD software Hoam-OpenCFD. *e-Sci. Technol. Appl.* **1**, 53–59.

LI, X.-L., LENG, Y. & HE, Z.-W. 2013 Optimized sixth-order monotonicity-preserving scheme by nonlinear spectral analysis. *Intl J. Numer. Meth. Fluids* **73** (6), 560–577.

LIU, J. & ZHANG, C. 2019 The fundamental secondary instability of the primary Mack mode in hypersonic boundary layers on flat plates. *Adv. Appl. Math. Mech.* **11**, 559–570.

MACK, L.M. 1984 Boundary-layer linear stability theory. *Tech. Rep.* AGARD 709. California Institute of Technology, Jet Propulsion Laboratory.

MAESTRELLO, L., BAYLISS, A. & KRISHNAN, R. 1991 On the interaction between first- and second-mode waves in a supersonic boundary layer. *Phys. Fluids* A **3** (12), 3014–3020.

MAYER, C.S.J., VON TERZI, D.A. & FASEL, H.F. 2011 Direct numerical simulation of complete transition to turbulence via oblique breakdown at Mach 3. *J. Fluid Mech.* **674**, 5–42.

MEERSMAN, J.A., HADER, C. & FASEL, H.F. 2021 Numerical investigation of nonlinear boundary-layer transition for cones at Mach 6. *AIAA J.* **59** (6), 1940–1952.

MORKOVIN, M.V. 1969 On the many faces of transition. In *Viscous Drag Reduction: Proceedings of the Symposium on Viscous Drag Reduction held at the LTV Research Center*, pp. 1–31. Springer.

NG, L.L. & ERLEBACHER, G. 1992 Secondary instabilities in compressible boundary layers. *Phys. Fluids* A **4** (4), 710–726.

ORSZAG, S.A. & PATERA, A.T. 1983 Secondary instability of wall-bounded shear flows. *J. Fluid Mech.* **128**, 347–385.

PRUETT, C.D. & CHANG, C.-L. 1995 Spatial direct numerical simulation of high-speed boundary-layer flows. Part 2. Transition on a cone in Mach 8 flow. *Theor. Comput. Fluid Dyn.* **7** (5), 397–424.

REN, J. & FU, S. 2014 Competition of the multiple Görtler modes in hypersonic boundary layer flows. *Sci. China-Phys. Mech. Astron.* **57** (6), 1178–1193.

REN, J., FU, S. & HANIFI, A. 2016 Stabilization of the hypersonic boundary layer by finite-amplitude streaks. *Phys. Fluids* **28** (2), 024110.

SCHNEIDER, S.P. 1999 Flight data for boundary-layer transition at hypersonic and supersonic speeds. *J. Spacecr. Rockets* **36** (1), 8–20.

SIVASUBRAMANIAN, J. & FASEL, H.F. 2015 Direct numerical simulation of transition in a sharp cone boundary layer at Mach 6: fundamental breakdown. *J. Fluid Mech.* **768**, 175–218.

THUMM, A. 1991 Numerische Untersuchungen zum laminar-turbulenten Strömungsumschlag in transsonischen Grenzschichtströmungen. PhD thesis, University of Stuttgart.

UNNIKRISHNAN, S. & GAITONDE, D.V. 2019 First-mode-induced nonlinear breakdown in a hypersonic boundary layer. *Comput. Fluids* **191**, 104249.

UNNIKRISHNAN, S. & GAITONDE, D.V. 2020 Linear, nonlinear and transitional regimes of second-mode instability. *J. Fluid Mech.* **905**, A25.

VAN DRIEST, E.R. 1951 Turbulent boundary layer in compressible fluids. *J. Aeronaut. Sci.* **18** (3), 145–160.

WHITE, F.M. 2006 *Viscous Fluid Flow*. McGraw-Hill.

YU, M. & LUO, J. 2014 Nonlinear interaction mechanisms of disturbances in supersonic flat-plate boundary layers. *Sci. China Phys. Mech. Astron.* **57**, 2141–2151.

ZAKI, T.A. & DURBIN, P.A. 2005 Mode interaction and the bypass route to transition. *J. Fluid Mech.* **531**, 85–111.

ZAKI, T.A. & DURBIN, P.A. 2006 Continuous mode transition and the effects of pressure gradient. *J. Fluid Mech.* **563**, 357–388.

ZHANG, C. & LUO, J. 2017 Selective enhancement of oblique waves caused by finite amplitude second mode in supersonic boundary layer. *Appl. Math. Mech.* **38** (8), 1109–1126.

ZHANG, C., ZHU, Y., CHEN, X., YUAN, H., WU, J., CHEN, S., LEE, C. & GAD-EL HAK, M. 2015 Transition in hypersonic boundary layers. *AIP Adv.* **5** (10), 107137.

ZHANG, C.-H., TANG, Q. & LEE, C.-B. 2013 Hypersonic boundary-layer transition on a flared cone. *Acta Mechanica Sin.* **29**, 48–54.

ZHAO, R., WEN, C., ZHOU, Y., TU, G.-H. & LEI, J.-M. 2022 Review of acoustic metasurfaces for hypersonic boundary layer stabilization. *Prog. Aerosp. Sci.* **130**, 100808.

ZHOU, T., LIU, Z., LU, Y., KANG, D. & YAN, C. 2022*a* Control of oblique breakdown in a supersonic boundary layer employed a local cooling strip. *J. Fluid Mech.* **949**, A4.

ZHOU, T., LIU, Z., LU, Y., WANG, Y. & YAN, C. 2022*b* Direct numerical simulation of complete transition to turbulence via first- and second-mode oblique breakdown at a high-speed boundary layer. *Phys. Fluids* **34** (7), 074101.

ZHOU, T., LIU, Z. & YAN, C. 2023 Linear and nonlinear instabilities of a high-speed boundary layer on porous coating. *AIAA J.* **61** (1), 489–496.

ZHOU, T., LU, Y., LIU, Z. & YAN, C. 2021 Direct numerical simulation of control of oblique breakdown in a supersonic boundary layer using a local cooling strip. *Phys. Fluids* **33** (8), 084101.

ZHU, Y., CHEN, X., WU, J., CHEN, S., LEE, C. & GAD-EL HAK, M. 2018 Aerodynamic heating in transitional hypersonic boundary layers: role of second-mode instability. *Phys. Fluids* **30** (1), 011701.

ZHU, Y., ZHANG, C., CHEN, X., YUAN, H., WU, J., CHEN, S., LEE, C. & GAD-EL HAK, M. 2016 Transition in hypersonic boundary layers: role of dilatational waves. *AIAA J.* **54** (10), 30.